TÉCNICO LISBOA

Partial power DC-DC converter to integrate PV systems in DC grids

João Maria Cunha Campos

Thesis to obtain the Master of Science Degree in

Electrical and Computer Engineering

Supervisors: Prof. Sónia Maria Nunes dos Santos Paulo Ferreira Pinto
Mestre Guilherme Marto Paraíso

Examination Committee

Chairperson: Prof. Célia Maria Santos Cardoso de Jesus
Supervisor: Prof. Sónia Maria Nunes dos Santos Paulo Ferreira Pinto
Member of the Committee: Prof. Vitor Manuel de Carvalho Fernão Pires

January 2021

Declaration

I declare that this document is an original work of my own authorship and that it fulfills all the requirements of the Code of Conduct and Good Practices of the Universidade de Lisboa.

Acknowledgments

This thesis represents the ending of an important chapter in my life and I couldn't have done it without the many people that have supported me throughout all of these years.

I would like to start by thanking my supervisors, Prof. Sónia Pinto and Guilherme Paraíso for their continuous help, availability and support even during such trying times as the unforeseen pandemic lockdown.

To my mother and brother, who were always present in my life despite of the distance, I owe a huge thanks for their unconditional support and love. I would also like to thank my family in Leiria and Benedita for always being there for me.

I would like to thank my friends, João and Tiago, I have made at Instituto Superior Técnico for making this journey worthwhile and to my long date friends, Miguel and Radu, for helping me no matter what.

I would also like to thank Carolina for her companionship and giving me strength and courage during these years and her family as well for their hospitality and kindness.

Finally, I would like to thank project PTDC/EEI-EEE/32550/2017- Smart Transformers for Sustainable Grids of Fundação para a Ciência e Tecnologia (FCT) which is related to my thesis research topic.

Resumo

O conceito de *Partial power processing* é aplicado a conversores de potência de forma a reduzir as suas perdas, tamanho e custos. Esta técnica consiste em projetar um conversor que processa uma fração da potência de entrada.

O objetivo desta dissertação é avaliar o rendimento e a resposta de um conversor parcial de potência quando inserido numa microrede DC. De forma a atingir este objetivo o conversor vai ser projetado e dimensionado para funcionar tanto como um conversor elevador para conectar um sistema fotovoltaico e como um conversor redutor para conectar uma carga de potência constante à microrede DC.

O sistema fotovoltaico consiste num único painel fotovoltaico e vai servir de elemento gerador na microrede. Um algoritmo MPPT é usado para garantir a máxima geração de potência. Outros elementos da microrede são os conversores, os filtros e as cargas de potência constante, e todos são dimensionados para integrar a microrede DC.

O controlo dos conversores é feito utilizando controladores não-lineares, uma alternativa ao clássico controlo linear escolhida pelo facto de os conversores também serem sistemas não-lineares. As técnicas de controlo usadas são o modo de deslizamento e o *backstepping* os quais se baseam na teoria de estabilidade de *Lyapunov*. Para servir de comparação um controlador linear foi desenhado para um dos conversores.

Com o fim de obter resultados toda a microrede DC foi modelada e simulada em *Matlab/Simulink* e testada para vários cenários diferentes, nos quais a resposta de todos os componentes da microrede DC foi avaliada.

Palavras-chave: Microrede DC, MPPT, Controladores não-lineares, Conversor parcial de potência, Sistema fotovoltaico.

Abstract

Partial power processing is a concept applied to power converters in order to reduce its losses, size and cost. This technique consists of designing a converter that only processes a fraction of the input power.

This dissertation's objective is to analyze the performance of a partial power converter when operating in a DC microgrid. For that purpose the partial power converter will be designed and sized to work as both a step-up converter and a step-down converter to connect a PV system and a constant power load, respectively, to the DC microgrid.

The PV system consists of a single PV panel and it operates as a generator element in the DC microgrid. An MPPT algorithm is used to guarantee maximum power generation. Other elements of the DC microgrid are the converters, filters and constant power loads, and all are designed and sized to integrate the DC microgrid.

The control of the converters is made using non-linear controllers, an alternative approach to the classic linear control chosen because of the inherent non-linearity of the converters. Both the backstepping technique and sliding mode control methods based on Lyapunov's stability theory were used. For comparison purposes one linear controller was designed for one of the converters.

In order to obtain results a DC microgrid was modelled and simulated in *Matlab/Simulink* for different operation scenarios, in which the performance of the DC microgrid components was evaluated.

Keywords: DC Microgrid, MPPT, Non-linear controllers, Partial Power Converter, PV system.

Table of Contents

Declaration ..... **i**

Acknowledgments ..... **iii**

Resumo ..... **v**

Abstract ..... **vi**

Table of Contents ..... **viii**

List of Figures ..... **x**

List of Tables ..... **xi**

List of Acronyms ..... **xii**

List of Symbols ..... **xiii**

1 Introduction **1**

1.1 Objectives 2

1.2 Thesis Organization 3

2 DC grid Converters **5**

2.1 Step-up Partial Power Converter 5

2.2 Step-down Partial Power Converter 11

2.3 Filters Design in the connection to the DC grid 15

2.4 Dual Active Bridge Converter 18

3 Photovoltaic Panel **21**

3.1 Theoretical model 21

3.2 I-V curve 23

3.3 Simulated Model 25

4 Controllers Design **27**

4.1 Maximum Power control - MPPT algorithm 27

4.2 Non-linear control methods 29

4.2.1 Lyapunov's Second Method 29

4.2.2 Backstepping technique 30

4.2.3 Sliding Mode Control 31
4.3 Step-up PPC control 32
4.3.1 Non-linear control 32
4.3.2 Linear control 36
4.4 Step-down PPC non-linear control 39
4.5 DAB non-linear control 42

5 Obtained results 45
5.1 Scenario 1 - PV panel operation in nominal conditions 45
5.2 Scenario 2 - PV panel operation with irradiance levels change 49
5.3 Scenario 3 - Stand-alone operation of constant power loads 52
5.4 Scenario 4 - DC grid behaviour when both PV panel and CPLs are connected and disconnected 54

6 Conclusions 57
6.1 Final Conclusions 57
6.2 Future Work 58

Bibliography 59

List of Figures

Fig. 1.1 Visualization of the partial power processing concept (taken from [1]). Power flow is split into two paths: one being a ”direct” path between source and output with negligible losses and the other path is the conversion stage. 1

Fig. 2.1 DC microgrid configuration. 5
Fig. 2.2 PV system connection to a DC grid using a flyback converter configuration. 6
Fig. 2.3 PV system connection to a DC grid using a flyback based partial power converter configuration. 6
Fig. 2.4 Step-up PPC current waveforms. 7
Fig. 2.5 Magnetizing current in inductance L_m while in steady-state operation. 9
Fig. 2.6 Current $i_{C_{pv}}$. 10
Fig. 2.7 Connection of the DC grid to a constant power load using a step-down PPC configuration. 11
Fig. 2.8 Step-down PPC current waveforms. 12
Fig. 2.9 Magnetizing current in inductance L_m while in steady-state operation (Step-down PPC). 13
Fig. 2.10 Current i_{C_o}. 14
Fig. 2.11 Output filter for the step-up PPC. 15
Fig. 2.12 Input filter for the step-down PPC. 16
Fig. 2.13 Comparison of unfiltered and filtered currents. 17
Fig. 2.14 Dual Active Bridge converter. 18
Fig. 2.15 Voltage v_{s1} and voltage v_{s2}. 19
Fig. 2.16 Voltage and current in L. 19
Fig. 2.17 DAB converter power in function of the phase shift φ. 19

Fig. 3.1 Diode and 5 parameters model. 21
Fig. 3.2 I-V and P-V curves of a photovoltaic panel (taken from [17]). 23
Fig. 3.3 Effects of Irradiance and Temperature on the I-V curve of a PV panel (taken from [18]). 24
Fig. 3.4 Effects of R_s, R_{sh} and temperature on the I-V curve of a PV panel (taken from [17]). 24

Fig. 4.1 Tracking of the MPP in the P-V curve by the P&O MPPT (taken from [19]). 28
Fig. 4.2 Flowchart of the Perturb & Observe MPPT algorithm. 28
Fig. 4.3 Nonlinear voltage controller. 34
Fig. 4.4 Sliding mode current controller. 36

Fig. 4.5 Voltage PI controller with limiter. 39
Fig. 4.6 Backstepping controller for the DAB converter. 44

Fig. 5.1 *MatLab/Simulink* model used for scenario 1 and 2. 45
Fig. 5.2 Comparison of voltage MPPT tracking of a non-linear controller and linear controller during nominal operation. 46
Fig. 5.3 Input PV power P_{pv}. 47
Fig. 5.4 Partial power ratio K_{pr} of the step-up PPC during nominal operation. 47
Fig. 5.5 Input power, output power and efficiency for nominal operation of the step-up PPC considering conduction and switching losses. 48
Fig. 5.6 Input power, output power and efficiency for nominal operation of the Flyback converter considering conduction and switching losses. 48
Fig. 5.7 Comparison of voltage MPPT tracking of a non-linear controller and linear controller for various irradiance levels. 50
Fig. 5.8 Comparison of voltage MPPT tracking of a non-linear controller and linear controller at a 200 W/m^2 irradiance level. 50
Fig. 5.9 Input PV power P_{pv} for the various irradiance levels. 51
Fig. 5.10 Partial power ratio K_pr of the step-up PPC for various irradiance levels. 51
Fig. 5.11 *MatLab/Simulink* model used for scenario 3. 52
Fig. 5.12 Output voltage for each of the constant power loads. 52
Fig. 5.13 Output power for each of the constant power loads. 53
Fig. 5.14 Partial power ratio of the step-down PPC for each of the constant power loads. . . . 53
Fig. 5.15 *MatLab/Simulink* model used for scenario 4. 54
Fig. 5.16 DC microgrid voltage and current during scenario 4 test. 55
Fig. 5.17 Power being processed by the DAB converter. 56
Fig. 5.18 PV voltage and load output voltages during scenario 4 test. 56

List of Tables

Table 2.1 Step-up PPC nominal operation parameters. 11
Table 2.2 Step-down PPC nominal operation parameters for 2 loads. 15
Table 2.3 Filters. 17
Table 2.4 DAB converter parameters. 20

Table 3.1 PV panel manufacturer's datasheet data. 25
Table 3.2 Diode and 5 parameters model calculated values. 25
Table 3.3 NOCT operating point values at irradiance = 800 W/m^2. 26

Table 4.1 Steady-state operation point used for linearization of step-up PPC. 38
Table 4.2 PI linear controller parameters. 39

Table 5.1 Non ideal elements used to model conduction losses in both converters. 47
Table 5.2 Differences between step-up PPC and flyback at nominal operation. 49
Table 5.3 Results for the scenario 2 test using the nonlinear controller. 51

List of Acronyms

AC	Alternating Current
CPL	Constant Power Load
DAB	Dual Active Bridge
DC	Direct Current
ESS	Energy Storage System
IGBT	Insulated Gate Bipolar Transistor
MOSFET	Metal Oxide Semiconductor Field Effect Transistor
MPP	Maximum Power Point
MPPT	Maximum Power Point Tracking
NOCT	Nominal Operating Cell Temperature
PI	Proportional-Integral
PPC	Partial Power Converter
PV	Photovoltaic
SMC	Sliding Mode Controller
STC	Standard Test Conditions

List of Symbols

A	Area of transversal section of the semiconductor
C_f	Input filter capacitor
C_g	Output capacitor of DAB converter
C_o	Output capacitor of Step Down PPC
C_{of}	Output filter capacitor
C_{pv}	Step-up PPC input capacitor
d	Ratio for which control objective is multiplied to obtain error bandwidth
D_1	step-up PPC diode
D_2	step-down PPC diode
e_x	Control error of variable x
f_{cf}	Cut-off frequency
f_s	Switching frequency
G_{fe}	Photoelectric effect generation current
G_v^*	Voltage gain
i_b	DAB converter input battery current
i_{Cpv} , i_{Co} , i_{Cg}	Capacitor currents
I_d	Diode current
i_{dc}	DAB converter second bridge output current
i_g	DAB converter output current
i_{in}	Step-up PPC input current
I_{INref}	Step-up PPC input current reference
i_L	DAB converter's inductor current
i_{load}	Step-down PPC output load current
i_{Lm}	Magnetizing inductance current
I_{mp}	PV panel current at maximum power
i_o	PPC output current
I_{Oref}	Step-down PPC output current reference
i_{pc}	PPC current
i_{pv}	PV panel current
I_s	Reverse saturation current
I_{sc}	Solar cell short circuit current
K^*	Boltzmann constant
K_{i1} , K_{i2} , K_{i3}	Backstepping integral control gain
K_{pr}^*	Partial power ratio
K_{v1} , K_{v2} , K_{v3}	Backstepping voltage control gain
k_p	Integral gain of voltage PI controller
k_p	Proportional gain of voltage PI controller
L_n	Diffusion length for electrons
L_p	Diffusion length for holes
L^*	DAB converter inductance
L_f^*	Input filter inductance

L_m^*	Magnetizing inductance
L_{of}^*	Output filter inductance
n	Transformer's turns ratio
n_{DAB}	DAB converter transformer's turns ratio
n^*	Diode ideality factor
N_p	Number of cells in parallel
N_s	Number of cells in series
P_{DAB}	DAB converter average power flow from the first bridge to the second bridge
P_f	Filter output power
P_{in}	Step-down PPC input power
P_{mp}	PV panel maximum power
P_o	Step-up PPC output power
P_{pc}	Power processed by the PPC
P_{pv}	PV panel power
P_{OUT}	Power consumed by CPL's
q	Electron charge
r_L	Inductor series resistance
R_o	Step-down PPC output resistance
R_{pv}	PV panel dynamic resistance
R_s	Solar cell contacts resistance
R_{sh}	Solar cell leakage resistance
s	Sliding surface
S_1	Step-up PPC MOSFET
S_2	Step-down PPC MOSFET
S_{11} , S_{12} , S_{13} , S_{14}	DAB converter first bridge IGBT's
S_{21} , S_{22} , S_{23} , S_{24}	DAB converter second bridge IGBT's
t	Time
T	Absolute temperature of solar cell
T_s^*	Switching period
u	Control input
u_t^*	Thermal voltage
V^*	Lyapunov function
V_b	DAB converter input battery voltage
V_{dc}	DC microgrid voltage
V_{DCref}	DC microgrid voltage reference
V_{Lm}	Average magnetizing inductance voltage
V_{mp}	PV panel maximum power
V_o	Average step-down PPC output voltage
V_{Oref}	Step-down PPC output voltage reference
V_{oc}	PV panel open circuit voltage
V_{pv}	PV panel voltage
V_{PVref}	PV panel voltage reference
v_L	DAB converter's inductor voltage
v_{Lm}	Magnetizing inductance voltage
v_o	Step-down PPC output voltage
v_p	DAB converter's primary voltage
v_{pc}	PPC voltage
v_{pRMS}	DAB converter's primary RMS voltage
v_{s1RMS}	DAB converter's secondary RMS voltage
v_{s1}	DAB converter's secondary voltage
v_{s2}	DAB converter's second bridge voltage

x	System state variable
x_{ref}	System state variable reference
δ	Duty-cycle
Δ	Bandwidth
Δi_{Lm} , Δi_{in} , Δi_{Lof} , Δi_{Lf}	Current ripples
Δv_{pv} , Δv_o , Δv_{Cof} , Δv_{Cf}	Voltage ripples
Δt	Interval of time
η	Efficiency
φ	Phase shift between square voltages of the DAB converter
τ	Time constant
ζ	Damping ratio

Chapter 1

Introduction

The technique of partial power processing consists of designing and sizing a converter to only process a fraction of the total power. This way the converter's losses, size and cost can be reduced. This technique is achieved by "splitting" the power flow into two paths: one being a series path between input and output and the other being the conversion stage. In Fig. 1.1 a representation of this concept is shown. This way the conversion stage can be sized for a smaller power which means that in comparison to a full power converter its semiconductors ratings can be reduced. If it is the case that a transformer is used in the conversion stage, its rating and size can also be reduced. These improvements potentially lead to an increase in the converter's efficiency and a reduction of its size and cost.

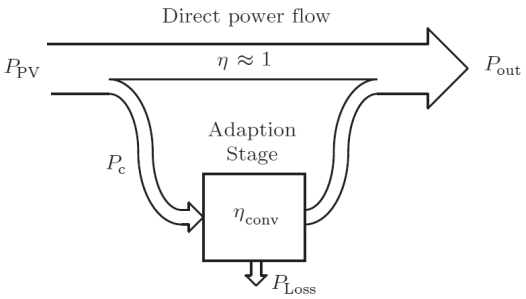

Figure 1.1: Visualization of the partial power processing concept (taken from [1]). Power flow is split into two paths: one being a "direct" path between source and output with negligible losses and the other path is the conversion stage.

The concept of Partial Power Converters (PPC) has been around for some time: in [2] a converter referred as Series Connect Boost Unit (SCBU) was presented for spacecraft applications. This converter achieved a high efficiency by using an isolated buck converter in series with the input voltage source which only processed a fraction of the total power. It must be noted that as more partial power processing architectures were presented along the years, the name SCBU became obsolete and many names have been used to refer to these types of converters, such as Partial Capacity Converter, Partial Power Processing Converters and Series Voltage Compensation [3]. This lack of agreement has been recognized in [4] and a unifying criteria for nomenclature has been proposed, however since it is out of the scope of this thesis to classify and analyze different PPC architectures the names of step-up and step-down PPC are chosen for simplicity.

More recently and focused in the problem of voltage mismatch between PV panels in a string (e.g. due

to shading), presented in [1] is a study of various PV panel integrated DC-DC converters where the technique of PPC is analyzed as one of the solutions. Several applications have been proposed that follow this concept, such as: the well-known doubly fed induction generator [5] for wind turbines, a DC bus regulator [6] for spacecraft applications or a DC-DC converter [7] for distributed PV architectures. The topology that this thesis focuses on is the one in [3] and [8] in which a PPC based on a Flyback converter is presented to integrate two-stage configurations (a first DC-DC stage to boost the voltage and a second DC-AC stage to connect to the grid). For the purpose of this thesis only the DC-DC stage is interesting since the PV system is being connected to a DC grid instead of an AC grid.

In the last few years DC grids have been suggested as an alternative to the traditional AC grid. In the past AC grids offered a clear advantage over DC in transmitting and distributing power due to the use of transformers. However, in recent times, thanks to the large developments of power electronics, DC systems have been increasing in use, and many of modern electrical loads, such as a variety of domestic appliances use DC power. Nowadays DC grids offer the possibility of increasing the efficiency, power quality and reliability over the existing AC grid [9]. Furthermore, renewable energy sources such as PV panels produce DC power and their integration is easier in DC grids.

The adoption of PV panels as an energy source has also seen a very positive increase in recent times. This growth is being driven by the effort to reduce fossil fuel consumption and environmental concerns while it is also being accompanied by a steady decrease in generation costs [10]. Since PV panels produce DC power they are commonly connected to a DC-DC stage that either connects them to an Energy Storage System (ESS) or to an AC-DC stage for grid connection. In the case of connection to a DC grid the AC-DC stage becomes unnecessary and so the DC-DC stage is sufficient to perform a connection. This DC-DC stage also guarantees that the PV system is working at maximum power through the use of a maximum power point tracking (MPPT) algorithm.

The proposed PPC fits in the DC grid as a solution capable of stepping up the voltage and therefore able to connect a PV panel to the grid. Additionally the same PPC topology will be used to connect a constant power load (CPL) to the grid, in this case working as step-down converter.

1.1 Objectives

The main goals of this thesis are to design and analyse a converter topology that uses the partial power processing technique:

- To integrate the PPC in a DC microgrid where it must be able to connect both a PV system and CPLs to the grid.

- To control the PV system to guarantee that it is working at maximum power (*Maximum Power Point Tracking*) at all time regardless of the irradiance level.

- To design the DC microgrid elements to assure their proper functioning, such as a converter to balance the power flow and set the grid voltage and finally filters for the converters.

- The used power electronic converters are highly non-linear systems due to high frequency switching of the semiconductors. To design non-linear controllers to address this issue as an alternative to the classic linear controllers.

- To simulate the PPC and the DC microgrid in *Matlab/Simulink* in order to obtain results of the performance of each element.

1.2 Thesis Organization

This thesis is divided into 6 chapters. This first one is introductory and presents the structure and objectives of the thesis.

In chapter 2 the components of the DC microgrid are designed and sized. These include a step-up PPC that connects the PV system to the grid, a step-down PPC to connect the grid to CPLs, a Dual Active Bridge converter that will balance the power flow in the grid and filters for the converters.

In chapter 3 the photovoltaic panel is studied. Its theoretical model is presented and analyzed, namely the solar cell, its I-V curve and its defining parameters. The simulated model used for testing is also presented.

In chapter 4 the control methodologies used for the converters and for the PV system are presented. The MPPT algorithm that guarantees the PV system is working at maximum power is shown, followed by the controllers design. These non-linear controllers are based on the Lyapunov stability theory.

In chapter 5 the obtained results from the simulation of the DC microgrid in *Matlab/Simulink* are shown, for different test scenarios.

Lastly, chapter 6 lists the main conclusions drawn from this dissertation in addition to suggesting possible future work ideas.

Chapter 2

DC grid Converters

This chapter focuses in the analysis and sizing of three converters, each with a different purpose in the DC microgrid. The first is the step-up PPC which connects the PV system to the microgrid, the second is the step-down PPC which connects constant power loads to the microgrid and finally the third converter is the one responsible for setting the microgrid voltage. All the converters and the overall DC microgrid configuration are represented in Fig. 2.1 .

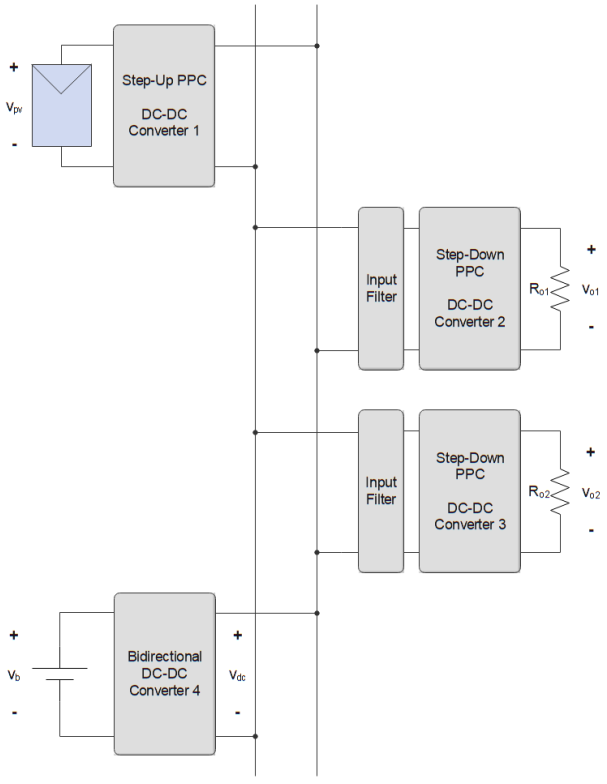

Figure 2.1: DC microgrid configuration.

2.1 Step-up Partial Power Converter

In order to connect the PV panel to the DC grid a step-up converter is needed to boost the voltage at the output of the panel. The DC grid operates at 380V while a 60 cell PV panel voltage ranges around 30V, so a high voltage gain is required. A popular choice for this scenario is the flyback converter, shown

in Fig. 2.2, since it presents high voltage gain, galvanic isolation and it is used for low power (200-300W). The used PPC topology is based on the flyback converter and inherits most of its characteristics except galvanic isolation. In Fig. 2.3 the PPC based on a flyback topology can be seen. A MOSFET semiconductor was chosen as the converter will operate at frequencies of 50 kHz and above.

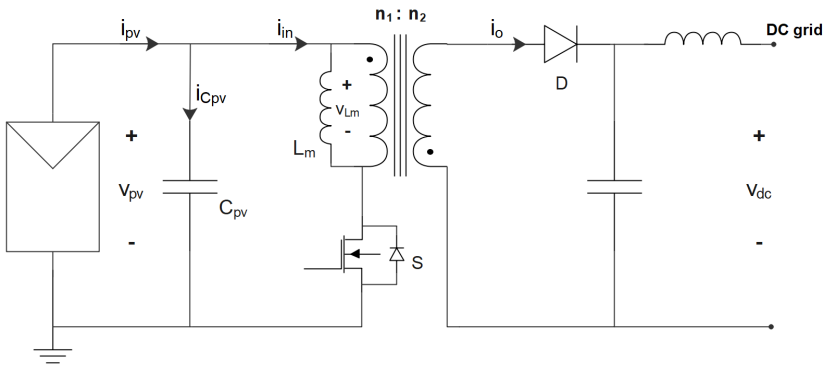

Figure 2.2: PV system connection to a DC grid using a flyback converter configuration.

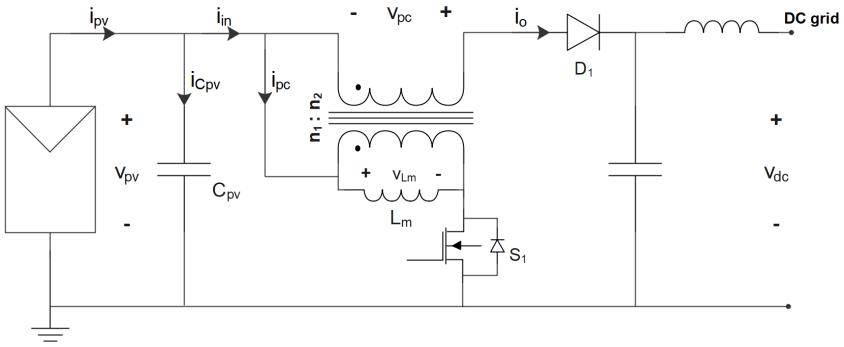

Figure 2.3: PV system connection to a DC grid using a flyback based partial power converter configuration.

In comparison to the flyback topology, by changing the connections of the transformer, the voltage across the secondary becomes a series voltage v_{pc}. Applying kirchoff's circuit laws we get (2.1) and (2.2).

$$V_{pv} + v_{pc} = V_{dc} \tag{2.1}$$

$$i_{pc} + i_o = i_{in} \tag{2.2}$$

This is a crucial difference between this topology and the flyback one: the voltage across the secondary of the flyback converter is equal to the output voltage whereas in the PPC converter the secondary's voltage is equal to the series voltage v_{pc}, which is lower than the output voltage.

The voltage v_{pc} and the voltage across the inductance L_m will depend on the state of the semiconductor switch S_1 and are given by (2.3) and (2.4) respectively, where n is the transformer's turns ratio $n = \frac{n_2}{n_1}$.

$$v_{pc} = \begin{cases} -n \cdot V_{pv} \ , & \text{if } S_1 \text{ ON} \\ V_{dc} - V_{pv}, & \text{if } S_1 \text{ OFF} \end{cases} \tag{2.3}$$

$$v_{L_m} = \begin{cases} V_{pv} \ , & \text{if } S_1 \text{ ON} \\ \dfrac{V_{pv} - V_{dc}}{n} \ , & \text{if } S_1 \text{ OFF} \end{cases} \tag{2.4}$$

Contrary to most isolated converters, the flyback converter stores energy in its transformer, normally through the use of an air gap, represented by the inductance L_m in Fig. 2.3. Also the flyback transformer's windings never conduct at the same time and so the transformer serves the purpose of storing magnetic energy through the use of its magnetizing inductance. In Fig. 2.4 the currents of the converter can be seen during steaty-state operation. The input current i_{in} is non-linear due to being the sum of currents with different magnitudes. This gap between i_{pc} and i_o is proportional to the turns ratio of the transformer.

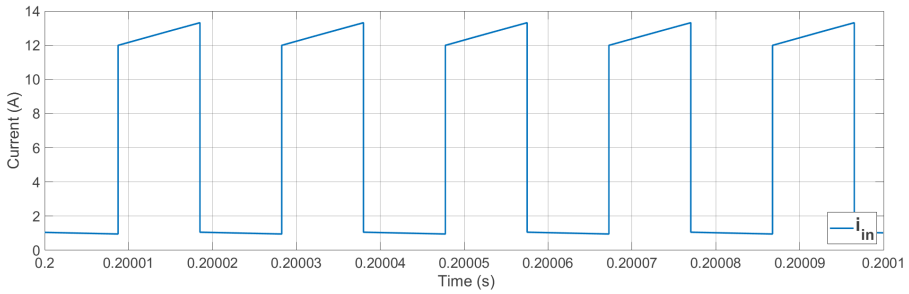

(a) Current i_{in}.

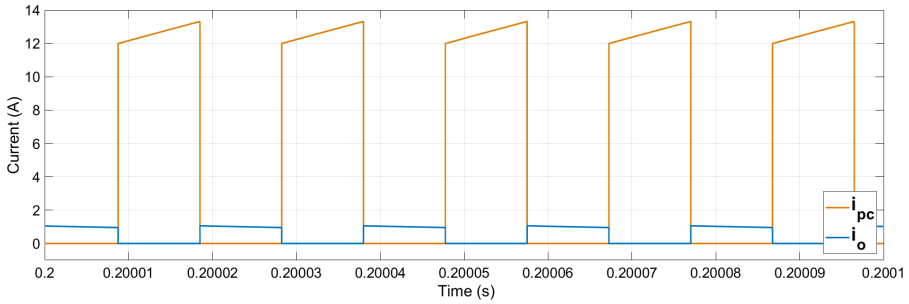

(b) Current i_{pc} (orange) and current i_o (blue).

Figure 2.4: Step-up PPC current waveforms.

$$G_{v_{flyback}} = n \cdot \frac{\delta}{1 - \delta} \tag{2.5}$$

In order to size the PPC converter we need to derive the input/output voltage relations. For comparison, the expression for the flyback converter voltage gain is (2.5), where δ is the duty-cycle of the switch. The gain for the PPC converter can be calculated from the average value of the voltage in the inductance.

As in steady-state the average voltage in the inductance is zero:

$$\begin{aligned} V_{L_m} = \frac{1}{T}\int_0^T v_{L_m}\,\mathrm{d}t = 0 \Leftrightarrow \\ \Leftrightarrow V_{pv}\cdot\delta + \frac{V_{pv}}{n}\cdot(1-\delta) - \frac{V_{dc}}{n}\cdot(1-\delta) = 0 \Leftrightarrow \\ \Leftrightarrow \frac{V_{dc}}{V_{pv}} = G_{v_{PPC}} = \frac{1+\delta(n-1)}{1-\delta} \Leftrightarrow \end{aligned} \tag{2.6}$$

The voltage gain necessary to connect the PV panel to the DC grid can be calculated by knowing the PV panel's operating point (discussed further in the next chapter). The MPP PV panel voltage, $V_{mp} = 28V$ can be used as the nominal value since it uses the PV panel's nominal operating cell temperature of 45ºC, which is a more realistic scenario than STC conditions of 25ºC cell temperature. This choice is relevant because while the cell temperature has a significant effect on voltage at MPP the level of irradiance has much less effect, as seen in Fig. 3.3. The output voltage will be the 380V DC grid's voltage and so the required voltage gain is:

$$G_{v_{PPC}} = \frac{V_{dc}}{V_{pv}} \tag{2.7}$$

Using this voltage gain as reference for the nominal operation of the converter the turns ratio of the transformer can be obtained. The duty-cycle δ desired during nominal operation should be around 50% since this is the duty-cycle that minimizes magnetic losses in the core for the flyback converter [11]. Solving (2.6) for n we get:

$$n = 1 + \frac{G_{v_{PPC}}(1-\delta) - 1}{\delta} \tag{2.8}$$

The authors of [3] and [8] present a parameter to analyze the power processed by the PPC, which is simply the ratio between the power processed by the converter and the power delivered by the PV system as in (2.9). This parameter will be a value below unity since the converter will process less power than the power supplied by the PV system.

$$K_{pr} = \frac{P_{pc}}{P_{pv}} \tag{2.9}$$

To calculate the K_{pr} for this converter the power $P_{pv} = V_{pv}I_{pv}$ and $P_{pc} = V_{pv}I_{pc}$, which are the power supplied by the PV system and the power processed by the PPC respectively, are used. The efficiency of the converter is calculated in (2.10), where P_o is the output power of the PPC.

$$\eta = \frac{V_{dc}\cdot I_{dc}}{V_{pv}\cdot I_{pv}} = \frac{P_o}{P_{pv}} \tag{2.10}$$

Then substituting (2.10) in (2.9) the value of K_{pr} for this converter is obtained (2.11). For this converter the K_{pr} depends on the voltage gain and efficiency of the converter.

$$\begin{aligned} K_{pr} &= \frac{P_{pc}}{P_{pv}} = \frac{V_{pv} \cdot I_{pc}}{V_{pv} \cdot I_{pv}} = \\ &= 1 - \frac{P_o}{V_{dc}} \cdot \frac{1}{\frac{P_{pv}}{V_{pv}}} \Leftrightarrow \\ \Leftrightarrow K_{pr} &= 1 - \frac{\eta}{G_{v_{PPC}}} \end{aligned} \tag{2.11}$$

The magnetizing inductance of the transformer also needs to be determined. In Fig. 2.5 the magnetizing current can be seen. In steady-state the average value of i_{L_m} will remain constant. However, the current waveform will present a triangular shape which is affected by the magnetizing inductance. Expression (2.12) is used to calculate the current ripple.

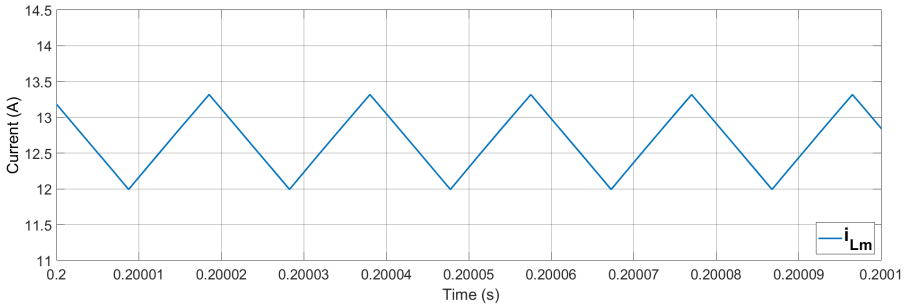

Figure 2.5: Magnetizing current in inductance L_m while in steady-state operation.

$$\Delta i_{L_m} = \frac{V_{pv} \cdot \delta \cdot T_s}{L_m} \tag{2.12}$$

The current ripple Δi_{L_m} in (2.12) still needs to be chosen in order to determine L_m. While the average current drawn from the PV panel is given by (2.13) the average current in L_m will be higher [12] and given by (2.14), after adjusting for a PPC configuration with a factor of K_{pr}.

$$I_{pv} = \frac{P_{pv}}{V_{pv}} \tag{2.13}$$

$$I_{L_m} = \frac{P_{pv}}{V_{pv} \cdot \delta} \cdot K_{pr} \tag{2.14}$$

Solving (2.12) and setting Δi_{L_m} to 10% of I_{L_m}, L_m is calculated:

$$L_m = \frac{V_{pv} \cdot \delta \cdot T_s}{\Delta i_{L_m}} \tag{2.15}$$

The sizing of the input capacitor takes into account the current ripple in i_{in} which is a non-linear current due to it switching between windings (Fig. 2.4a). Applying Kirchhoff's Current law, $i_{C_{pv}}$ is given by (2.16) and its waveform can be seen in Fig. 2.6.

$$i_{C_{pv}} = i_{pv} - i_{in} \tag{2.16}$$

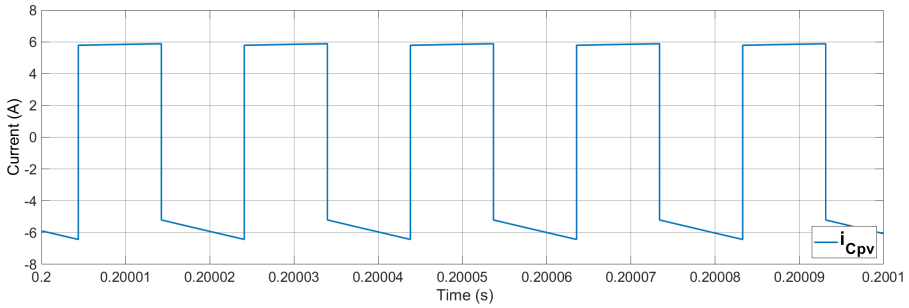

Figure 2.6: Current $i_{C_{pv}}$.

Since current i_{pv} is a slow changing current with a small ripple, it's only needed to determine the ripple of current i_{in}, which is given by (2.17) and (2.18). The transformer's turn ratio is needed since i_{in} is flowing through the secondary winding of the transformer when switch S_1 is OFF.

$$i_{in} = \begin{cases} i_{L_m}\ , & \text{if } S_1 \text{ ON} \\ \dfrac{i_{L_m}}{n}\ , & \text{if } S_1 \text{ OFF} \end{cases} \tag{2.17}$$

$$\Delta i_{in} = \left(I_{L_m} + \frac{\Delta i_{L_m}}{2} \right) - \left(\frac{I_{L_m} - \frac{\Delta i_{L_m}}{2}}{n} \right) \tag{2.18}$$

The output capacitor will be sized assuming steady state operation and so it can be given by expression (2.19):

$$i_{Cpv} = C_{pv} \cdot \frac{\mathrm{d}V_{pv}}{\mathrm{d}t} \approx C_{pv} \cdot \frac{\Delta V_{pv}}{\Delta t} \Rightarrow I_{Cpv} = C_{pv} \cdot \frac{\Delta V_{pv}}{\Delta t} \Rightarrow C_{pv} = \frac{I_{Cpv} \cdot \delta T_s}{\Delta V_{pv}} \tag{2.19}$$

Even though the average value of current i_{Cpv} is zero in steady state, it oscillates around zero with a peak-to-peak amplitude of Δi_{in} and its waveform somehow resembles a square waveform. For the purpose of the sizing the input capacitor i_{Cpv} is approximated to a square waveform centered in zero and with a value of $\frac{\Delta i_{in}}{2}$ when S_1 is ON and $-\frac{\Delta i_{in}}{2}$ when S_1 is OFF. Assuming a maximum ripple of 2% in V_{pv}, C_{pv} can be calculated by the following equation:

$$C_{pv} = \frac{\frac{\Delta i_{in}}{2} \cdot \delta T_s}{\Delta V_{pv}} \tag{2.20}$$

In table 2.1 all the relevant calculated parameters for the step-up PPC can be found.

Table 2.1: Step-up PPC nominal operation parameters.

Nominal Operation Parameters	
Input voltage V_{pv} [V]	28
Input current I_{pv} [A]	6.7
Output voltage V_{dc} [V]	380
Output current I_{dc} [A]	0.48
Duty-Cycle [%]	50
Switching frequency f_s [kHz]	50
Partial power ratio K_{pr}	0.9263
Transformer's turns ratio, n	12.57
Magnetizing inductance L_m [μH]	225
Input Capacitor C_{pv} [μF]	108

2.2 Step-down Partial Power Converter

In the proposed DC grid the loads are connected to the DC microgrid through a step-down converter to reduce the voltage to 48V or 24V. The configuration chosen is the same used for the step-up PPC except it was modified so that the power could flow in the opposite direction - the MOSFET and the diode switched positions - as can be seen in Fig. 2.7. This converter will operate at 100 kHz and for that reason a MOSFET is chosen.

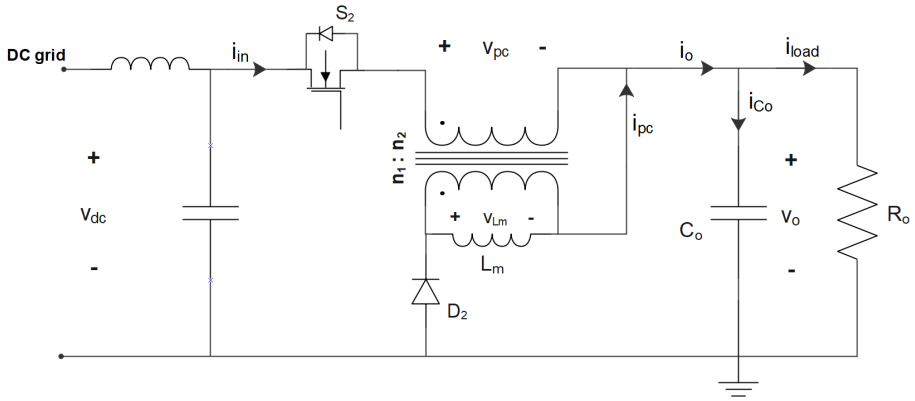

Figure 2.7: Connection of the DC grid to a constant power load using a step-down PPC configuration.

Applying kirchoff's circuit laws we get (2.21) and (2.22):

$$v_o + v_{pc} = V_{dc} \tag{2.21}$$

$$i_{in} + i_{pc} = i_o \tag{2.22}$$

The voltage v_{pc} and the voltage of the inductance L_m will depend on the state of the semiconductor S_2 and are given by (2.23) and (2.24) respectively. The expressions for this converter aren't much different from the ones in the step-up PPC and the waveform of the currents i_o, i_{in} and i_{pc} can be seen in Fig. 2.8.

$$v_{pc} = \begin{cases} V_{dc} - v_o \ , & \text{if } S_1 \text{ ON} \\ -n \cdot v_o, & \text{if } S_1 \text{ OFF} \end{cases} \tag{2.23}$$

$$v_{L_m} = \begin{cases} \dfrac{V_{dc} - v_o}{n} \ , & \text{if } S_1 \text{ ON} \\ -v_o \ , & \text{if } S_1 \text{ OFF} \end{cases} \tag{2.24}$$

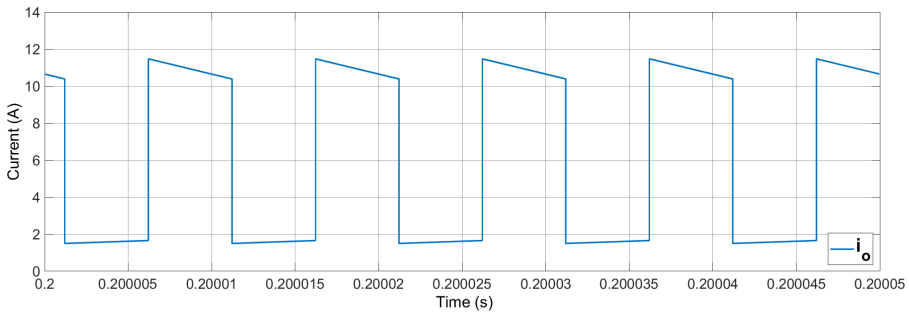

(a) Current i_o.

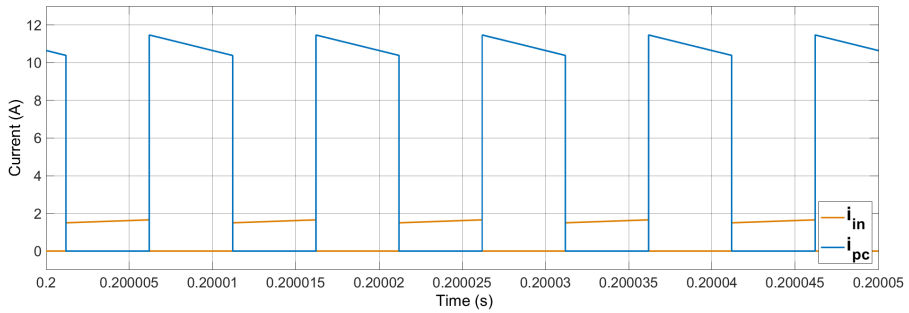

(b) Current i_{in} (orange) and current i_{pc} (blue).

Figure 2.8: Step-down PPC current waveforms.

Several parameters need to be determined and sized for the nominal operating point. The load is assumed to be operating at constant power, a Constant Power Load (CPL), as is the case in most electronic loads. Two constant power loads will be connected to the DC grid, the first one is a 300W load operating at 48V whereas the second one is a 200W load at 24V. The voltage gain of the converter is calculated by averaging the magnetizing inductance voltage over one period in steady-state (2.25).

$$\begin{aligned} V_{L_m} = \ & \frac{1}{T} \int_0^T v_{L_m} \, \mathrm{d}t = \ 0 \Leftrightarrow \\ \Leftrightarrow \ & \frac{(V_{dc} - V_o)}{n} \cdot \delta - V_o \cdot (1 - \delta) = \ 0 \Leftrightarrow \\ \Leftrightarrow \ & \frac{V_o}{V_{dc}} = G_{v_{PPC}} = \frac{\delta}{\delta + n(1 - \delta)} \Leftrightarrow \end{aligned} \tag{2.25}$$

From (2.25) the voltage gain is then given by (2.26):

$$G_{v_{PPC}} = \frac{V_o}{V_{dc}} \tag{2.26}$$

The transformer's turn ratio can be determined by solving (2.25) for n and choosing a duty-cycle of 50%:

$$n = \frac{\delta \cdot (1 - G_{v_{PPC}})}{G_{v_{PPC}} \cdot (1 - \delta)} \tag{2.27}$$

To calculate the value of K_{pr}, the power definitions $P_{pc} = V_{pc} I_{in}$ and $P_{in} = V_{dc} I_{in}$, which are the power processed by the PPC and the input power of the converter respectively, are used:

$$\begin{aligned} K_{pr} &= \frac{P_{pc}}{P_{in}} = \frac{V_{pc} \cdot I_{in}}{V_{dc} \cdot I_{in}} = \\ &= \frac{V_{dc} - V_o}{V_{dc}} = 1 - \frac{V_o}{V_{dc}} = \\ &\Leftrightarrow K_{pr} = 1 - G_{v_{PPC}} \end{aligned} \tag{2.28}$$

The magnetizing current of this PPC can be seen in Fig. 2.9 and its average value is given by (2.29), similarly to the step-up PPC magnetizing current.

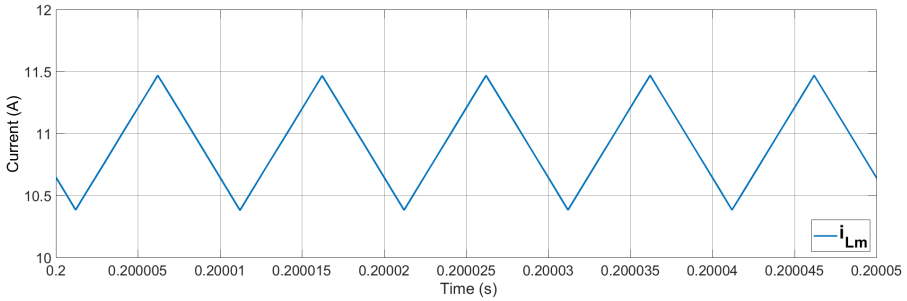

Figure 2.9: Magnetizing current in inductance L_m while in steady-state operation (Step-down PPC).

$$I_{L_m} = \frac{P_{in}}{V_o \cdot \delta} \cdot K_{pr} \tag{2.29}$$

$$\Delta i_{L_m} = \frac{V_o \cdot \delta \cdot T_s}{L_m} \tag{2.30}$$

The current ripple in L_m when the semiconductor switch S_2 is OFF is given by (2.30) which solving for L_m can be written as:

$$L_m = \frac{V_o \cdot \delta \cdot T_s}{\Delta i_{L_m}} \tag{2.31}$$

The output capacitor needs to be sized according to the ripple of a non-linear current, this case current i_o. Applying Kirchhoff's Current law, i_{C_o} is given by (2.32) and its waveform can be seen in Fig. 2.10.

$$i_{C_o} = i_o - i_{load} \tag{2.32}$$

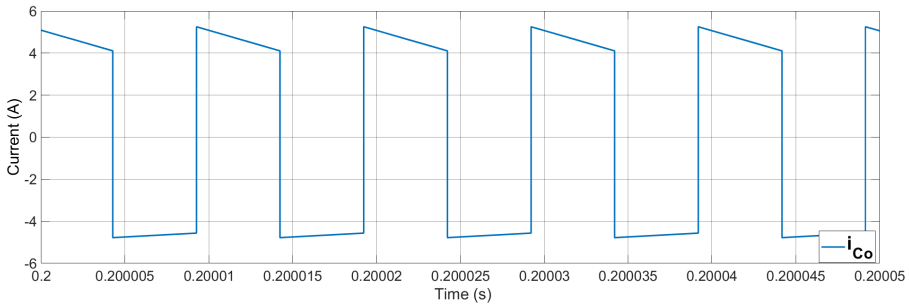

Figure 2.10: Current i_{C_o}.

The output current i_o is given by (2.33) and its ripple, or peak-to-peak amplitude, is given by (2.18), the same expression used for i_{in} in the step-up PPC.

$$i_o = \begin{cases} \frac{i_{L_m}}{n}, & \text{if } S_1 \text{ ON} \\ i_{L_m}, & \text{if } S_1 \text{ OFF} \end{cases} \tag{2.33}$$

The output capacitor C_o is determined in the same way as in the step-up PPC (2.19):

$$C_o = \frac{I_{Co} \cdot \delta T_s}{\Delta V_o} \tag{2.34}$$

The current i_{C_o} will also be approximated to a square wave for the purpose of sizing C_o - centered around zero with a value of $\frac{\Delta i_o}{2}$ when S_1 is OFF and $-\frac{\Delta i_o}{2}$ when S_1 is ON. From (2.34) capacitance C_o is determined:

$$C_o = \frac{\frac{\Delta i_o}{2} \cdot \delta T_s}{\Delta V_o} \tag{2.35}$$

All the relevant parameters determined and sized for the step-down converter can be seen in table 2.2. The table is divided in two, the left side is for the 300W load and the right side is for the 200W load. A ripple of 10% was considered to size the filtering inductances and a ripple of 1% was considered to size the filtering capacitors.

Table 2.2: Step-down PPC nominal operation parameters for 2 loads.

Converter parameters for 300W load	
Input voltage V_{dc} [V]	380
Input current I_{dc} [A]	0.79
Output voltage V_{o1} [V]	48
Output current I_{load} [A]	6.25
Duty-Cycle [%]	50
Switching frequency f_s [kHz]	100
Partial power ratio K_{pr}	0.8737
Transformer's turn ratio, n	6.92
Magnetizing inductance L_m [μH]	220
Output Capacitor C_o [μF]	52

Converter parameters for 200W load	
Input voltage V_{dc} [V]	380
Input current I_{dc} [A]	0.53
Output voltage V_{o2} [V]	24
Output current I_{load} [A]	8.33
Duty-Cycle [%]	50
Switching frequency f_s [kHz]	100
Partial power ratio K_{pr}	0.9368
Transformer's turn ratio, n	14.83
Magnetizing inductance L_m [μH]	77
Output Capacitor C_o [μF]	160

2.3 Filters Design in the connection to the DC grid

The output current of the step-up PPC (Fig. 2.4b) and the input current of the step-down PPC (Fig. 2.8b) are high-ripple switching currents with a high harmonic content which is not desirable to inject in the DC grid. For that reason, and to minimize the ripple of the currents injected and supplied from the DC grid low-pass filters are used in the step-up and step-down PPC.

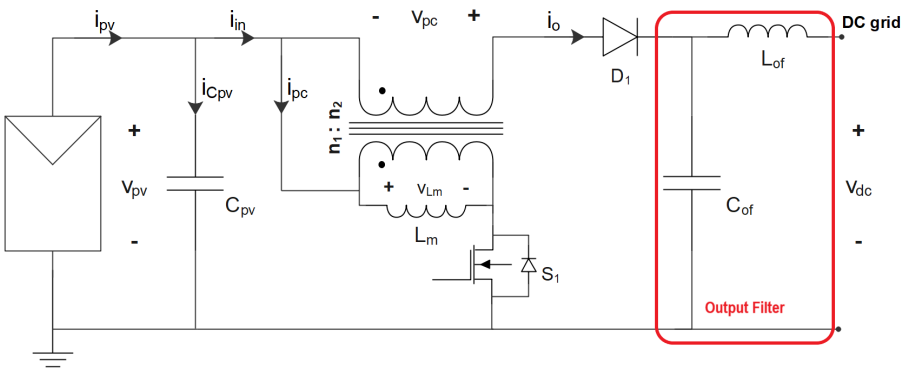

Figure 2.11: Output filter for the step-up PPC.

In Fig. 2.11 the LC output filter used for the step-up PPC can be seen. The capacitor can be sized using (2.36), where I_o is the average value of the output current and $\Delta v_{C_{of}}$ is the ripple of the capacitor voltage. The voltage across the inductor L_{of} is given by (2.37) and is equal to the difference between the capacitor C_{of} voltage and the DC grid voltage, and its maximum value is half of the ripple in the capacitor's voltage, $\frac{\Delta v_{C_{of}}}{2}$. This voltage is used to obtain the expression for the inductance L_{of} (2.38).

$$C_{of} = \frac{I_o \cdot \delta T_s}{\Delta v_{C_{of}}} \tag{2.36}$$

$$v_{L_{of}} = L_{of} \cdot \frac{\mathrm{d}i}{\mathrm{d}t} = v_{C_{of}} - V_{dc} \tag{2.37}$$

$$L_{of} = \frac{\Delta v_{C_{of}} \cdot \delta T_s}{2 \cdot \Delta i_{L_{of}}} \tag{2.38}$$

Contrary to the step-up PPC, the step-down PPC needs an input filter, as in Fig. 2.12, since the switched current is in the input side. The value of the capacitance C_f and the inductance L_f are (2.39) and (2.40), respectively [13].

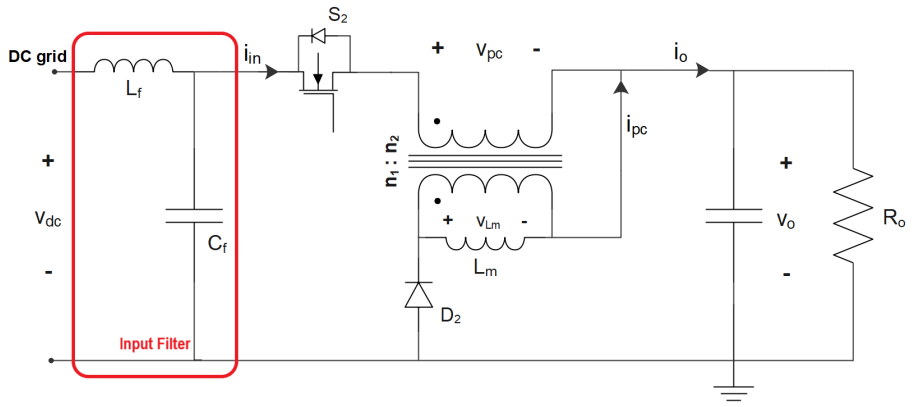

Figure 2.12: Input filter for the step-down PPC.

$$C_f = \frac{I_o \cdot T_s}{4 \cdot \Delta v_{C_f}} \tag{2.39}$$

$$L_f = \frac{T_s \cdot \Delta v_{C_f}}{8 \cdot \Delta i_{L_f}} \tag{2.40}$$

Although not shown in the figures a series resistance was added to the inductor to dampen the oscillations and avoid the system becoming unstable [13]. Taking into account the power the filter outputs P_f and its efficiency η_f, resistance r_L must respect condition (2.41):

$$r_L > \frac{L_f \cdot P_f}{C_f \cdot \eta_f \cdot V_{dc}^2} \tag{2.41}$$

The values for the filtering components are presented in table 2.3 and in Fig. 2.13 the comparison between filtered and unfiltered currents is observed. It can be seen that the filters are able to remove the high frequency ripple of the switching currents and transform them into suitable currents for the DC grid.

Table 2.3: Filters.

Output Filter for the step-up PPC	
Capacitor C_{of} [μF]	1.4
Inductor L_{of} [μH]	400
Inductor resistance r_L [Ω]	0.5

Input Filter (300W load)	
Capacitor C_f [μF]	4
Inductor L_f [μH]	60
Inductor resistance r_{L2} [Ω]	0.07

Input Filter (200W load)	
Capacitor C_{f2} [μF]	5.5
Inductor L_{f2} [μH]	90
Inductor resistance r_{L3} [Ω]	0.07

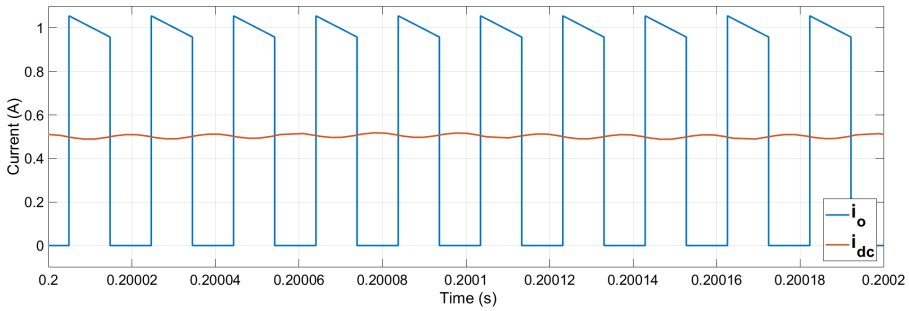

(a) Step-up PPC - unfiltered current i_o (blue) and filtered current i_{dc} (orange).

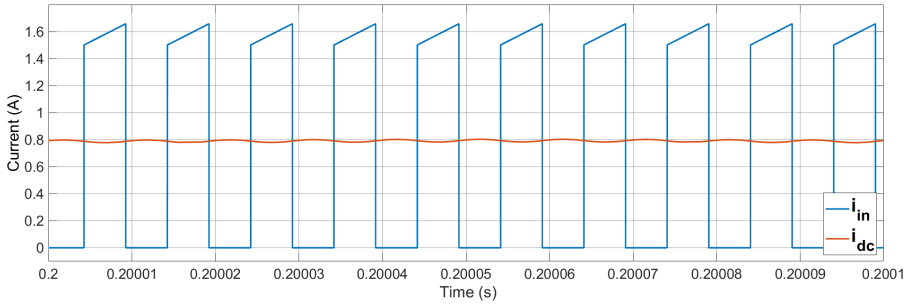

(b) Step-down PPC - unfiltered current i_{in} (blue) and filtered current i_{dc} (orange).

Figure 2.13: Comparison of unfiltered and filtered currents.

2.4 Dual Active Bridge Converter

All the converters designed so far have been used to connect either a power source (PV panel) or a load to the DC microgrid. The following converter is the one responsible for maintaining the DC grid voltage and balancing the power flow in the grid. The power flow needs to be balanced because in most cases the power being generated by the PV system does not match the power being consumed by the loads. It makes use of a 48V voltage source to either absorb or generate power, according to the difference of power being generated and consumed in the microgrid. The converter chosen for this purpose is the Dual Active Bridge (DAB) converter and its topology is shown in Fig. 2.14.

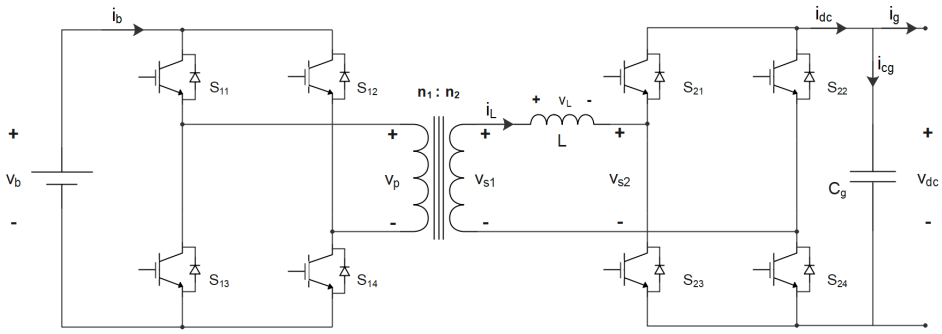

Figure 2.14: Dual Active Bridge converter.

The DAB converter is composed of two full bridges each connected to one of the sides of an high frequency transformer. The transformer provides galvanic isolation and voltage matching between two voltage levels, and inductor L represents the transformer's leakage inductances. Since it is represented in the secondary side, it is the sum of the secondary inductance, L_s, and the primary leakage inductance, L_p, referred to the secondary - $L = L_s + L_p \cdot n^2$.

Each full bridge consists of four semiconductors with turn-off capability and with diodes connected in anti parallel. In this case IGBTs were used due to the high power requirements and a switching frequency of 25 kHz. The first bridge connects a battery of voltage V_b to the primary side of the high frequency transformer and operates at a 50% duty-cycle producing an AC square wave voltage v_p. The second bridge, connected to the secondary side of the high frequency transformer, also operates at a 50% duty-cycle but with a phase shift φ in regards to the the first bridge. This creates the AC square wave voltage v_{s2}. The voltages at the inductor L terminals are $v_{s1} \approx nv_p$ and v_{s2}, respectively (Fig. 2.15), which result in the voltage across L of $v_L = v_{s1} - v_{s2}$ (Fig. 2.16). By controlling the phase shift between the two square wave voltages, the second bridge is able to control the average power flow from the first bridge to the second bridge as expressed in (2.42) [14] [15] and shown in figure Fig. 2.17.

$$P_{DAB} = \frac{nV_pV_{s2}}{2\pi^2 fL} \cdot \varphi(\pi - \varphi) \tag{2.42}$$

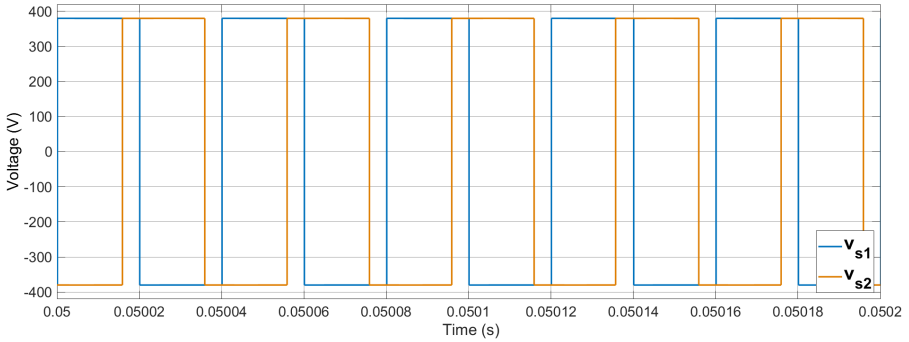

Figure 2.15: Voltage v_{s1} and voltage v_{s2}.

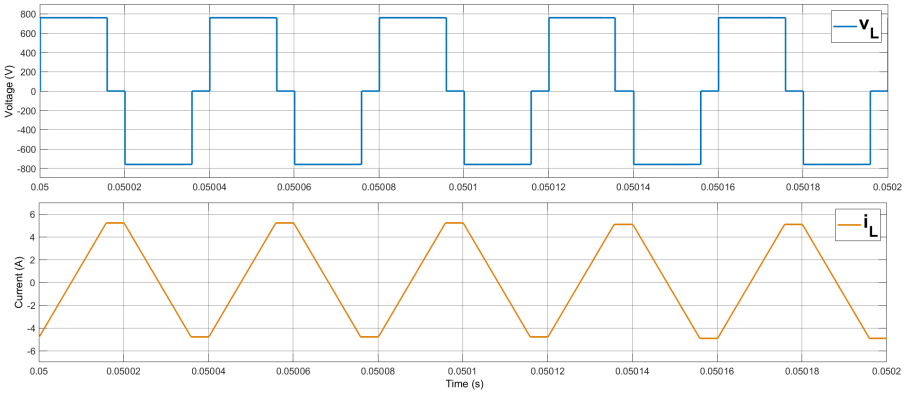

Figure 2.16: Voltage and current in L.

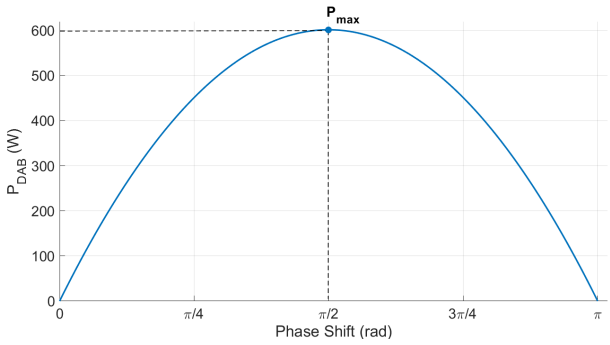

Figure 2.17: DAB converter power in function of the phase shift φ.

The transformer's turns ratio, $n_{DAB} = \dfrac{n_2}{n_1}$, will be sized in order to match the two voltage levels and it can expressed as:

$$n_{DAB} = \frac{V_{s1_{RMS}}}{V_{p_{RMS}}} = \frac{V_{dc}}{V_b} \tag{2.43}$$

The value of L is calculated considering the maximum power transferred which corresponds to a phase shift of $\frac{\pi}{2}$. The DAB is sized to 600W (Fig. 2.17), 100W above its maximum load, since it will have at most a 300W and a 200W load operating at the same time, which means a maximum load of 500W. Then solving (2.42) for L:

$$L = \frac{nV_p \cdot V_{s2}}{8fP_{max}} \tag{2.44}$$

The parameters determined for the DAB converter are shown in table 2.4.

Table 2.4: DAB converter parameters.

Input voltage V_b [V]	48
Output voltage V_{dc} [V]	380
Switching frequency f_s [kHz]	25
Transformer's turns ratio, n_{DAB}	7.92
Leakage inductance L [mH]	1.2
Output capacitor C_g [μF]	250

These values will be further used in the simulations.

Chapter 3

Photovoltaic Panel

A PV panel is divided into photovoltaic modules which are then divided into photovoltaic cells. In most commercial solutions these cells are made of silicon and are further N-type doped (electrons as majority carriers) and P-type doped (holes as majority carriers) to form a P-N junction. In this P-N junction an electric field is created, directed from the N side to the P side. By being exposed to light, either sunlight or artificial light, electron-hole pairs will be created which will generate an electric current when the terminals of the PV panel are connected to an external load. This is called the photovoltaic effect and it is responsible for the conversion of light into electric energy.

3.1 Theoretical model

To represent mathematically the photovoltaic effect two models stand out: the first one is the diode and 3 parameters and the second one is the diode and 5 parameters [16] [17]. The latter is chosen because in comparison to the 3 parameters model it represents ohmic losses in the contacts (through the resistance R_s) and leakage current losses (through the resistance R_{sh}). The model of the diode and 5 parameters can be seen in Fig. 3.1.

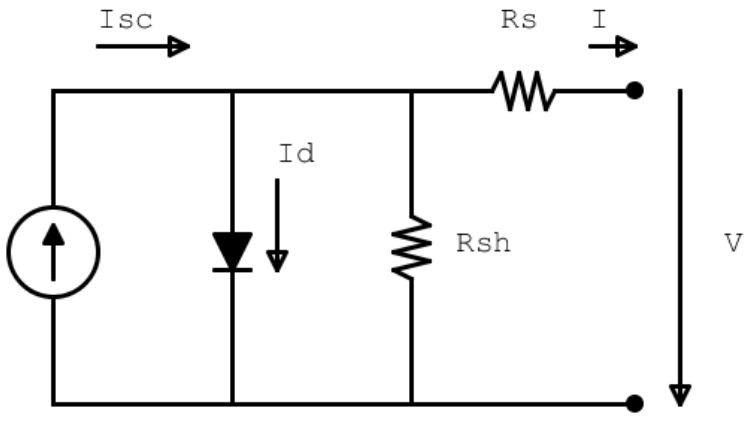

Figure 3.1: Diode and 5 parameters model.

The I_{sc} is the short circuit current generated by the solar cell when the voltage at its terminals is $V = 0$. It depends on the irradiance on the solar cell, the physical structure of the device and the semiconductors

used. It is given by (3.1), where q is the electron charge, G_{fe} is the photoelectric effect generation rate, L_p and L_n are diffusion lenghts for the holes and electrons, respectively, and A is the area of transversal section of the semiconductor.

$$I_{sc} = q\, G_{fe}(L_p + L_n)A \tag{3.1}$$

The junction p-n is a diode and generates a current, I_d, when a voltage V is applied across its terminals, and is given by (3.2) where I_s is the reverse saturation current, n is the diode ideality factor and u_T is the thermal voltage (3.3) which depends on the *Boltzmann* constant K, the absolute temperature of the solar cell T and the electron charge q.

$$I_d = I_S \left[\exp\left(\frac{IR_s + V}{nu_T}\right) - 1\right] \tag{3.2}$$

$$u_T = \frac{KT}{q} \tag{3.3}$$

As said previously the model chosen for the solar cell includes the losses in the solar cell's contacts, represented by R_s and losses through leakage currents, represented by R_{sh}. In order to reduce losses R_s should have a low value and R_{sh} a high value.

The load current is described by (3.4) in which I_d can be replaced by (3.2) and so we get (3.5).

$$I = I_{sc} - I_d - \left(\frac{IR_s + V}{R_{sh}}\right) \tag{3.4}$$

$$I = I_{sc} - I_S \left[\exp\left(\frac{IR_s + V}{nu_T}\right) - 1\right] - \left(\frac{IR_s + V}{R_{sh}}\right) \tag{3.5}$$

To summarize, the 5 parameters that define the model are:

- I_{sc} - the photovoltaic cell short-circuit current
- I_S - the diode reverse saturation current
- n - the diode ideality factor
- R_s - contact losses series resistance
- R_{sh} - leakage current losses parallel resistance

3.2 I-V curve

Since a photovoltaic panel is an association of photovoltaic cells in series and parallel, the voltage of the panel will depend on N_s, the number of cells in series, and the current on N_p, the number of cells in parallel. Fig. 3.2 shows both the I-V curve (in black) and P-V curve (in purple) of a PV panel. These curves are usually drawn for STC (standard test conditions) in which the panel is subject to the following conditions:

- Irradiance of 1000 W/m^2
- Cell temperature of 25 $C°$

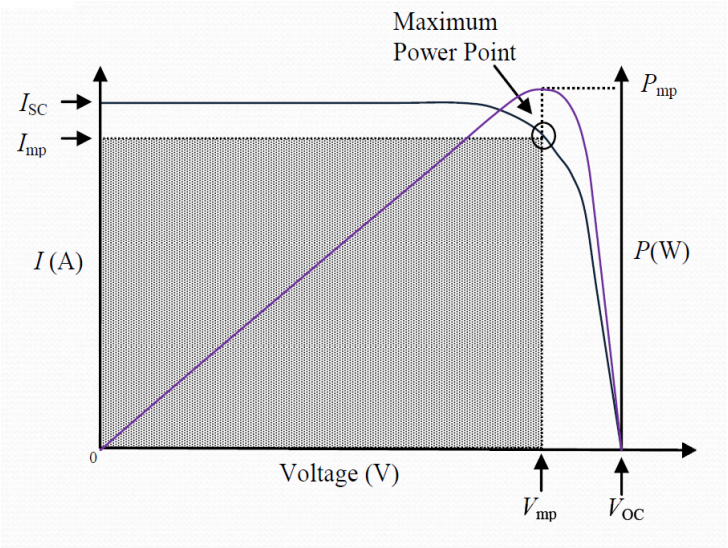

Figure 3.2: I-V and P-V curves of a photovoltaic panel (taken from [17]).

From these curves the following parameters can be retrieved:

- I_{SC} - the PV panel current when voltage is $V = 0$.
- I_{mp} - the PV panel current when its operating at maximum power.
- V_{OC} - the PV panel voltage when current is $I = 0$.
- V_{mp} - the PV panel voltage when its operating at maximum power.
- P_{mp} - the PV panel power at its maximum power point.

The operation of the panel will be influenced by several factors but more importantly by irradiance and cell temperature. The manufacturer's datasheet for PV panels often comes with the impact of the irradiance and temperature on the I-V curve. The PV panel chosen was the model CS6P-260 from the manufacturer *Canadian Solar* and Fig. 3.3, taken from the PV panel datasheet [18], shows the effects of irradiance (left-side graph) and temperature (right-side graph) in the I-V curve.

It can be seen in Fig. 3.3 that when irradiance increases so does the I_{SC} while V_{OC} remains almost the same. In contrast, with the increase of temperature, I_{SC} slightly increases while V_{OC} decreases significantly. This means that higher irradiances will lead to higher power generated, because the current at MPP (Maximum Power Point) will increase. On the other hand higher cell temperatures will lead to lower power generation, because the voltage at MPP will decrease at a rate higher than the current will

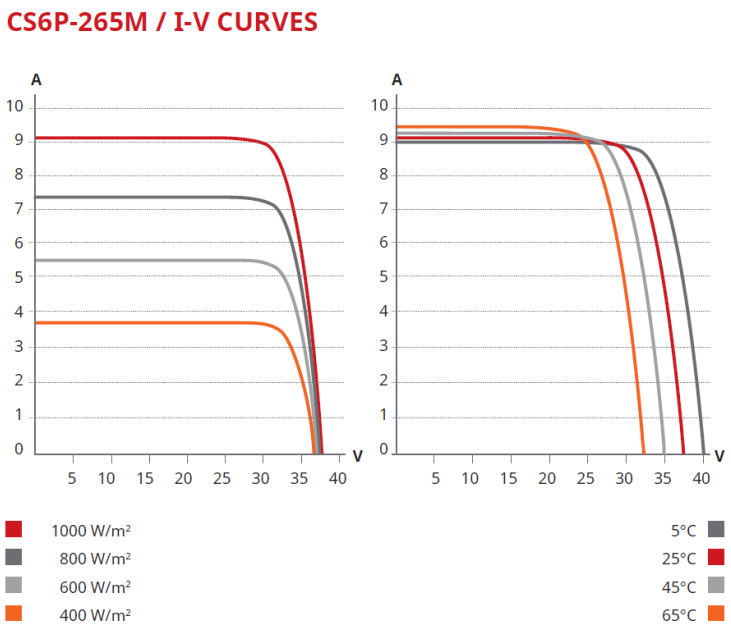

Figure 3.3: Effects of Irradiance and Temperature on the I-V curve of a PV panel (taken from [18]).

increase. The parameters used to describe the effect of temperature are the temperature coefficient of I_{SC} $(\%/C°)$ which is positive and temperature coefficient of V_{OC} $(\%/C°)$ which is negative.

Regarding the I-V curve of a PV panel and its performance it is also relevant to point out the effects of the series resistance R_s and parallel resistance R_{sh}. Fig. 3.4 (a) shows the effect of R_s and (b) shows the effect of R_{sh}. It is clear that both the increase of R_s and the decrease of R_{sh} flatten out the ”knee” of the I-V curve which means the MPP will be lower than before (the MPP is located around the ”knee” of the I-V curve). Fig. 3.4 (c) shows once more the effect of temperature already seen in Fig. 3.3. Note that these curves are in the 4th quadrant instead of the 1st because the authors used a different convention for the current.

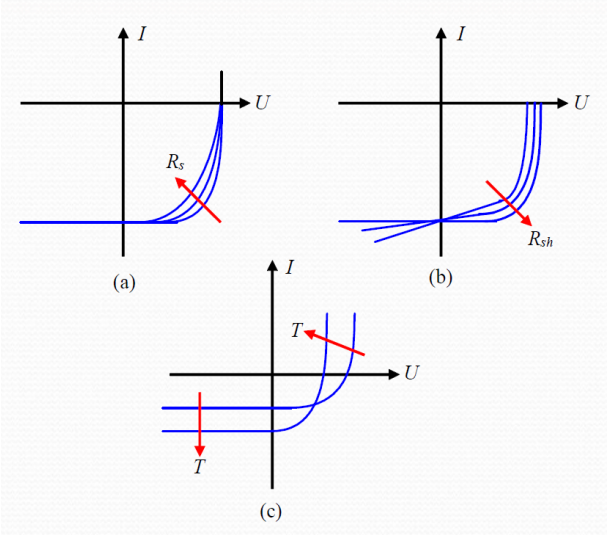

Figure 3.4: Effects of R_s, R_{sh} and temperature on the I-V curve of a PV panel (taken from [17]).

3.3 Simulated Model

The PV panel used in the simulated DC microgrid is an element in the library of the Matlab tool Simulink called ”PV Array”. This element uses the diode and 5 parameters model described in section 3.1. Simulink has a database of several PV panels from various brands or if the user prefers custom values can be added to simulate a custom PV panel. From the parameters described in section 3.2) : I_{SC}, I_{mp}, V_{OC}, V_{mp}, P_{mp} and the temperature coefficient of I_{SC} $(\%/C^{\circ})$ and V_{OC} $(\%/C^{\circ})$ at STC (standard test conditions) this element is then able to calculate the 5 parameters of the model. Table 3.1 shows the parameters taken from the PV panel's datasheet [18] that will be used by the ”PV array” element to calculate the 5 model parameters. The calculated parameters can be seen in table 3.2.

Table 3.1: PV panel manufacturer's datasheet data.

Number of Cells	60
P_{mp} [W]	260
I_{mp} [A]	8.48
V_{mp} [V]	30.7
I_{SC} [A]	8.99
V_{OC} [V]	37.8
Temp. coef. of I_{SC} $[\%/C^{\circ}]$	0.06
Temp. coef. of $V_{OC}[\%/C^{\circ}]$	-0.35

Table 3.2: Diode and 5 parameters model calculated values.

Diode and 5 parameters model	
I_{sc} [A]	9.01
I_S [A]	1.56e-10
n	0.98
R_s [Ω]	0.3
R_{sh} [Ω]	412

It is worth mentioning that STC conditions are very rarely achieved outside laboratory conditions and instead the following conditions are more realistic:

- Nominal operating cell temperature (NOCT) - 45 $\pm$ 2 C°
- Irradiance of 800 W/m^2

These conditions will set the best scenario for power generation of the PV panel. The performed simulations will keep the NOCT constant while changing the value of the irradiance between 200 W/m^2 (lowest power generated) and 800 W/m^2 (matching the conditions just described and resulting in the highest power generated). In table 3.3 the values for PV panel operating in these conditions can be seen. These

values were taken from the PV panel datasheet and are confirmed in the simulations (results in Chapter 5).

Table 3.3: NOCT operating point values at irradiance = 800 W/m^2.

NOCT operating point	
P_{mp} [W]	188
I_{mp} [A]	6.7
V_{mp} [V]	28.0
I_{SC} [A]	7.28
V_{OC} [V]	34.7

Chapter 4

Controllers Design

In this chapter the control strategies used for the several systems in the DC microgrid are developed. The PV system must always work in its maximum power point of operation and a MPPT algorithm is presented, followed by the control methods used for the converters. For all the converters nonlinear control methods are used and for the step-up PPC a linear PI controller is designed for comparison purposes.

4.1 Maximum Power control - MPPT algorithm

As described in section 3.2, a PV panel's power generation is not only dependent on external conditions, irradiance and cell temperature but also on its operating point (given by its voltage and current levels). In order to extract the maximum power from the PV panel in different conditions of irradiance and temperature a maximum power point tracking (MPPT) algorithm must be designed and implemented to make sure that the PV panel finds and tracks its maximum power point (MPP).

One of the most widely used MPPT algorithms is the Perturb & Observe (P&O) algorithm because of its effectiveness, simplicity and ease of implementation. It works by either making a positive or negative change in the PV panel's voltage or current and then checking if the power delivered increases or decreases. If it increases a change with the same direction is made, otherwise the voltage/current will be changed in the opposite direction. Because of this the MPPT will make adjustments in PV panel's voltage/current until it reaches the MPP and when it does it will start oscillating around that point. In Fig. 4.1 the P-V curve of the panel is used to demonstrate how the P&O MPPT operates when the voltage is being controlled. The direction of change in the MPPT's voltage reference depends in PV panel's current voltage value, i.e. if it is below or above the voltage at MPP. A more complete visualization of the MPPT algorithm can be seen through its flowchart in in Fig. 4.2.

This algorithm is straightforward as only operations of multiplication, comparison, addition and subtraction are needed. This makes it a low complexity process and easy to implement. The only parameters to be chosen when implementing this MPPT are the magnitude of change (the voltage step) to apply, and the period between changes, or the MPPT period. The following values were chosen:

- Voltage step, ΔV of 0.5V
- MPPT period of 5 ms

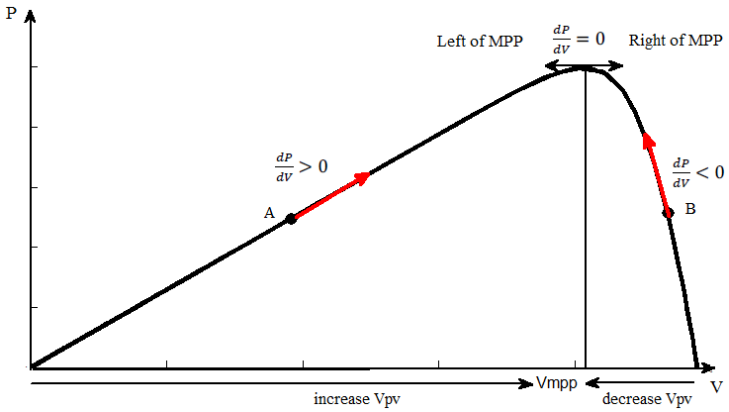

Figure 4.1: Tracking of the MPP in the P-V curve by the P&O MPPT (taken from [19]).

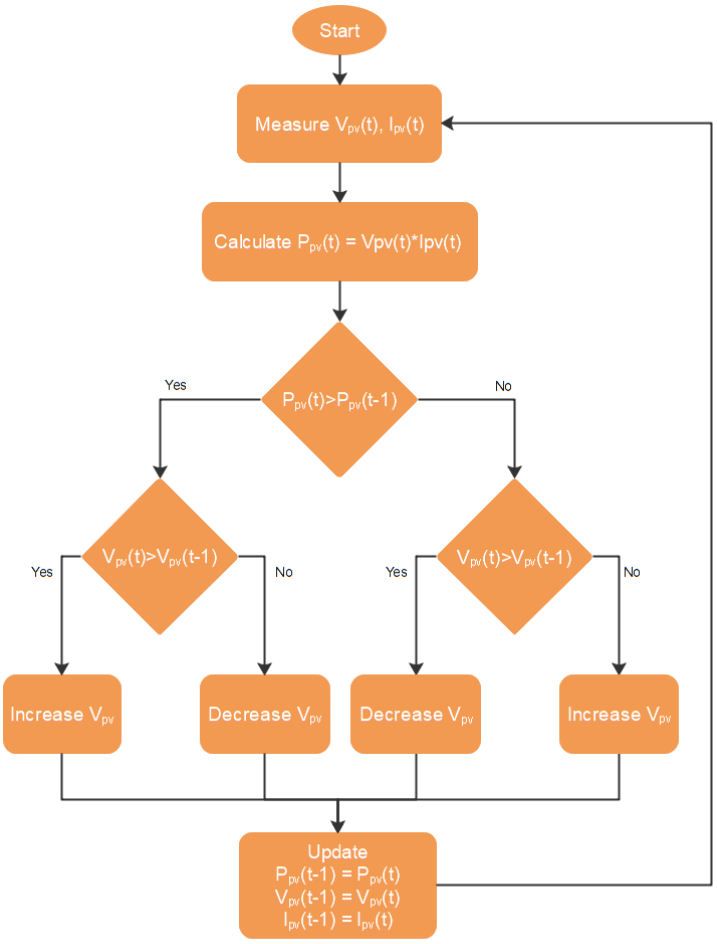

Figure 4.2: Flowchart of the Perturb & Observe MPPT algorithm.

Since the proposed PV system works in the range of 30V, a voltage step of 0.5V is enough. In PV systems where the working voltages are much higher the voltage step could be increased to improve the time it takes to the MPPT to reach MPP. The MPPT period must be high enough for the PV system and its controller to react to a new voltage reference [20] so that when a new change in the PV voltage is requested by the MPPT the PV system has already reached the previous reference.

4.2 Non-linear control methods

The converters studied in this work are all nonlinear systems. This requires the system to be linearized to apply classical control methods. The problem with this linearization is that it is done for a certain operation point and for large deviations from this point the controller's performance worsens. An alternative is to use non-linear control methods as the backstepping technique and sliding mode control. Both these methods are used to design the controllers of the converters along with the use of Lyapunov's second method to assure the stability of the system.

The control objective of the designed nonlinear controllers is to track either a voltage or current reference and as the actual voltage or current will never be exactly equal to the reference, an error value can be taken from the difference between the two:

$$e_x = x_{\text{ref}} - x \tag{4.1}$$

4.2.1 Lyapunov's Second Method

The control objective is to make the error value converge to zero and remain there. This means that the point $e_x = 0$ is an asymptotically stable equilibrium point. In order to make the control objective asymptotically stable Lyapunov's Second Method is used.

This method makes use of Lyapunov functions in which the error will be an argument. The Lyapunov function, V_v, is a positive definite, radially unbounded function which means it must satisfy the following conditions:

$$\begin{aligned} &\bullet\ V_v(e_x = 0) = 0 \\ &\bullet\ V_v(e_x \neq 0) > 0 \\ &\bullet\ V_v(|e_x| \to \infty) \to \infty \end{aligned} \tag{4.2}$$

And, additionally, to assure asymptotic stability:

$$\bullet\ \dot{V}_v(e_x \neq 0) < 0 \tag{4.3}$$

By using a Lyapunov function that satisfies these conditions and guarantees asymptotic stability the control objective, $e_x = 0$, is assured to be an asymptotically stable equilibrium point. An example of a Lyapunov function would be:

$$V_v = \frac{1}{2} e_x^2 \tag{4.4}$$

4.2.2 Backstepping technique

Even though the control objective of all controllers in this thesis is to track a voltage reference, all of them include an inner control loop for the current where the reference is calculated from the value of voltage error. This is achieved by using a technique similar to backstepping which makes use of Lyapunov functions.

Applying this technique to a nonlinear system breaks it down in smaller subsystems for which control laws can be obtained [21] [22]. The system can be broken down until the desired subsystem is reached, which might be the one with the control input or the one with the desired variable to control. Consider the following non-linear system:

$$\begin{aligned} \dot{x}_1 &= f_1(x_1) + g_1(x_1)x_2 \\ \dot{x}_2 &= f_2(x_1, x_2) + g_2(x_1, x_2)u \end{aligned} \tag{4.5}$$

Where (x_1,x_2) are the system variables, g_i(x_1,x_2) $\neq 0$ and u is the control input. The objective is to guarantee that system state x_1 tracks a reference signal x_{1ref} ($x_1 \rightarrow x_{1ref}$). The tracking error is defined as:

$$e_1 = x_{1ref} - x_1 \tag{4.6}$$

Then, the derivative of the error can be written according to (4.7), using (4.5) in (4.6).

$$\dot{e}_1 = \dot{x}_{1ref} - f_1(x_1) + g_1(x_1)x_2 \tag{4.7}$$

Now the system state x_2 acts as a virtual input for the subsystem in (4.7). A signal reference x_{2ref} can be chosen to make the $\dot{e}_1$ subsystem asymptotically stable. Using the following Lyapunov function:

$$V_1 = \frac{1}{2}e_1^2 \tag{4.8}$$

Which derivative is:

$$\dot{V}_1 = e_1\dot{e}_1 \tag{4.9}$$

Substituting $\dot{e}_1$ in (4.9) with (4.7) it is obtained:

$$\dot{V}_1 = e_1(\dot{x}_{1ref} - f_1(x_1) + g_1(x_1)x_2) \tag{4.10}$$

Similarly to system state x_1, an error is also defined for system state x_2:

$$e_2 = x_{2ref} - x_2 \tag{4.11}$$

This error is now used to rewrite (4.10):

$$\dot{V}_1 = e_1(\dot{x}_{1ref} - f_1(x_1) + g_1(x_1)(x_{2ref} - e_2)) \tag{4.12}$$

Expression (4.12) needs to satisfy condition (4.3), so the following constraint is applied:

$$\dot{V}_1 = -c_1 e_1^2 \,,\; c_1 > 0 \tag{4.13}$$

Where c_1 is greater than zero. Then first intermediate control law is obtained using (4.12) and (4.13):

$$x_{2ref} = \frac{1}{g_1(x_1)}(e_1 c_1 - f_1(x_1) + \dot{x}_{1ref}) \tag{4.14}$$

Enforcing error e_2 to go to zero by using this reference will also ensure that error e_1 converges to zero. The process described above could be repeated to obtain the final control law which includes the control input u but this technique is mainly used in this work to obtain a current reference from a voltage error and this analysis exemplifies that case.

4.2.3 Sliding Mode Control

To design the sliding mode controller two steps must be taken [22]: the first is to determine the sliding surface and the second is to establish the control laws that will make the system converge into the sliding surface and remain there.

In this work the sliding mode controllers are used to force a current to track a reference signal. As the current has a strong relative degree of one, then the sliding surface depends directly on the error of the current:

$$s(i) = e_i = I_{ref} - i \tag{4.15}$$

After identifying the sliding surface, Lyapunov's second method can be applied to drive the system towards it. Using the following Lyapunov function:

$$V_v = \frac{1}{2}s^2 \tag{4.16}$$

This function satisfies (4.2) and to guarantee stability it must also satisfy (4.3), resulting in:

$$\dot{V}_v = s\dot{s} < 0 \tag{4.17}$$

The system's dynamics, determined by the state of the semiconductor, is then analyzed to determine the control law. The states of the semiconductor are chosen in order to fulfill condition (4.17). In the case of this work only two states exist because only one semiconductor with switching off capability is present in the converters where this controller is used. For that reason, the possible states are "Switch ON" or "Switch OFF".

Ideally the system would reach the sliding surface and achieve zero error ($s(i) = 0$), changing between the states of the semiconductor switch at an infinite frequency in order to do so. However, due to physical limitations of the semiconductors, the switching frequency is limited and so is the sliding surface within an interval Δ around zero $-\frac{\Delta}{2} < s(i) < \frac{\Delta}{2}$. The width of this interval determines the switching frequency of the converter - the smaller it is the higher the frequency will be.

4.3 Step-up PPC control

Two different controllers are designed for the step-up PPC converter. The first is a nonlinear controller which uses an external loop for the voltage using the backstepping technique and internal loop for current using sliding mode control. The second one is a classic PI linear voltage controller.

4.3.1 Non-linear control

The voltage to be controlled in the step-up PPC is the PV panel voltage, which is the input voltage of the converter (Fig. 2.3). The error e_{Vpv} is then defined as:

$$e_{Vpv} = V_{PVref} - V_{pv} \tag{4.18}$$

The integral error of the voltage is also defined:

$$e_{I1} = \int_0^t e_{Vpv}\, \mathrm{d}t \tag{4.19}$$

The integral error is used to assure zero steady-state error that may occur due to parameters mismatch. Combining the two errors a Lyapunov function is proposed:

$$V_{v1} = K_{I1} \cdot \frac{e_{I1}^2}{2} + \frac{e_{Vpv}^2}{2}\ ,\ K_{I1} > 0 \tag{4.20}$$

Where K_{I1} is a constant greater than zero. This function satisfies the conditions in (4.2) for a Lyapunov function and its time derivative is:

$$\dot{V}_{v1} = K_{I1} \cdot e_{I1} \cdot \frac{de_{I1}}{dt} + e_{Vpv} \cdot \frac{de_{Vpv}}{dt} = K_{I1} \cdot e_{I1} \cdot e_{Vpv} + e_{Vpv} \cdot \frac{de_{Vpv}}{dt} \tag{4.21}$$

To guarantee asymptotic stability it must also satisfy (4.3) and so the following constraint is applied :

$$\dot{V}_{v1} < 0 \Rightarrow K_{I1} \cdot e_{I1} \cdot e_{Vpv} + e_{Vpv} \cdot \frac{de_{Vpv}}{dt} = -K_{v1} \cdot e_{Vpv}^2 \ , \ K_{v1} > 0 \tag{4.22}$$

As explained in section 4.1 the time response of the voltage must be faster than the MPPT period. Looking at (4.22) and focusing on the value of K_{v1} which determines the speed at which steady-state is reached [22] (e_{I1} is ignored in this analysis since it serves to correct the error at steady-state error) the following differential equation is reached:

$$\frac{de_{Vpv}}{dt} = -K_{v1} \cdot e_{Vpv} \ , \ K_{v1} > 0 \tag{4.23}$$

For which the solution is:

$$e_{Vpv} = ce^{-K_{v1}t} \tag{4.24}$$

Where K_{v1} is related to the time constant $\tau = \frac{1}{K_{v1}}$ and c is a constant. Since the MPPT period is 5ms the time period must be lower than that but higher than the inner current loop [22] which operates at 50 kHz. So τ must be between $1/50000 < \tau < 5ms$ - the value chosen for K_{v1} is 20000 (τ = 0.05ms).

Applying the backstepping technique it is possible to break down the system into a smaller subsystem. Analysing equation (4.25) that describes the dynamics of the input voltage, the main idea is to design a control law for the current so that the voltage's error converges to zero. Since the input voltage is equal to voltage of the input capacitor its derivative can be derived from its current:

$$\frac{dV_{pv}}{dt} = \frac{i_{Cpv}}{C_{pv}} = \frac{i_{pv} - i_{in}}{C_{pv}} \tag{4.25}$$

Now the derivative of the error e_{Vpv} can be determined:

$$\frac{de_{Vpv}}{dt} = \frac{dV_{PVref}}{dt} - \frac{i_{pv} - i_{in}}{C_{pv}} \tag{4.26}$$

By using (4.26) in (4.22) and solving for the current i_{in} the control law for that current is obtained:

$$I_{INref} = i_{pv} - C_{pv}\left(K_{v1} \cdot e_{Vpv} + K_{I1} \cdot e_{I1} + \frac{dV_{PVref}}{dt}\right) \tag{4.27}$$

The use of a Lyapunov function, along with the manipulation of the system's equations, breaks down the system into a lower order subsystem. This subsystem gives a control law for the current and if that current is controlled to follow its reference so is the voltage reference. After this step, the same process could be applied recursively to each outer subsystem until the final control law for the control input is obtained, however, in this case a new method for controlling the current was chosen. Fig. 4.3 shows the obtained nonlinear voltage controller. It contains an input rate limiter to prevent the derivative of the reference to be infinite and an output limiter to prevent the current reference from reaching undesired values (e.g. due to a large disturbance in the voltage error).

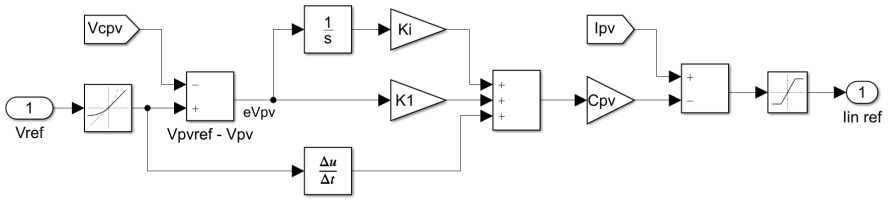

Figure 4.3: Nonlinear voltage controller.

The inner loop controls the input current of the converter and uses sliding mode control. Since the control objetive is $i_{in} = I_{INref}$ the sliding surface of the controller is the error associated with this current, which is to be kept in the vicinity of zero.

$$s(i_{in}) = e_{Iin} = I_{INref} - i_{in} \tag{4.28}$$

In order to determine the control law, the dynamics of the input current i_{in} is calculated using (2.4) and (2.17) resulting in (4.29).

$$\frac{di_{in}}{dt} = \begin{cases} \dfrac{di_{L_m}}{dt} = \dfrac{v_{pv}}{L_m}\,, & \text{if } S_1 \text{ ON} \\ \dfrac{\frac{di_{L_m}}{dt}}{n} = \dfrac{v_{pv} - v_{dc}}{n^2 L_m}\,, & \text{if } S_1 \text{ OFF} \end{cases} \tag{4.29}$$

As the DC grid voltage, v_{dc} , is always higher than the PV voltage, v_{pv} , the derivative of the input current has different signs according to the state of the semiconductor switch:

$$\begin{cases} \dfrac{di_{in}}{dt} > 0 \Rightarrow \dfrac{de_{Iin}}{dt} < 0\,, & \text{if } S_1 \text{ ON} \\ \dfrac{di_{in}}{dt} < 0 \Rightarrow \dfrac{de_{Iin}}{dt} > 0\,, & \text{if } S_1 \text{ OFF} \end{cases} \tag{4.30}$$

From (4.30) the state of the semiconductor can be chosen in order to satisfy condition (4.3), or in this case $e_{Iin} \cdot \frac{de_{Iin}}{dt} < 0$:

$$\begin{cases} e_{Iin} > 0 \rightarrow \dfrac{de_{Iin}}{dt} < 0 \rightarrow S_1 \text{ ON} \\ e_{Iin} < 0 \rightarrow \dfrac{de_{Iin}}{dt} > 0 \rightarrow S_1 \text{ OFF} \end{cases} \tag{4.31}$$

As explained previously the surface can't be exactly zero otherwise the switching frequency would need to be infinite. An interval centered around zero must be determined. For most surfaces this interval can be a percentage of the signal's reference (e.g. $\pm$ 5%-10%), however, due to the behaviour of the current i_{in} another solution is presented.

As was shown in Fig. 2.4a during the step-up PPC converter analysis, the input current is discontinuous as the result of being the sum of the two winding currents of the transformer. Consequently when the state of the semiconductor switch changes the current suffers a significant discontinuous increase/decrease. The difference of magnitude between the winding currents of the transformer increases as turns ratio increases and since the turns ratio of the transformers used in this work is not 1:1 there is always a difference between the currents. This difference is reflected in current i_{in} and must be accounted for. Specifically, the acceptable error interval needs to include the difference between the winding currents.

If the error interval is not large enough to account for this difference what would happen is that, as soon as the system changes state as a result of the switch changing its state, the current i_{in} would change value and immediately surpass the error interval boundaries triggering another change of state which would again make the current change value and cross the error interval boundary, repeating this behaviour indefinitely. This is undesirable as it would contribute to highly increase the semiconductors switching frequency.

Considering the upper boundary of the current, it must be high enough so that when it is divided by the transformer turns ratio it is still higher than the lower boundary. This results in the condition (4.32) where the minimum ratio d, for which the current reference can be multiplied, is obtained.

$$\begin{aligned} \frac{I_{INref} + I_{INref} \cdot \frac{d}{2}}{n} \geq I_{INref} - I_{INref} \cdot \frac{d}{2} \Leftrightarrow \\ \Leftrightarrow d \geq \ 2 \cdot \frac{n-1}{n+1} \end{aligned} \tag{4.32}$$

A minimum error ripple is defined as $\Delta_{\text{min}} = I_{INref} \cdot d$. This ripple is then increased $\Delta = \Delta_{\text{min}} + \Delta_{\text{add}}$, through the use of the term Δ_{add} to match the desired switching frequency, in this case 50 kHz for

nominal operation of the PV panel. Finally the control law is obtained as presented in (4.31):

$$\begin{cases} e_{Iin} > \dfrac{\Delta}{2} \rightarrow \dfrac{de_{Iin}}{dt} < 0 \rightarrow S_1 \text{ ON} \\ e_{Iin} < -\dfrac{\Delta}{2} \rightarrow \dfrac{de_{Iin}}{dt} > 0 \rightarrow S_1 \text{ OFF} \end{cases} \tag{4.33}$$

Regarding the switching frequency it must also be noted that as the PV panel deviates from nominal operation so will its current, meaning that if the irradiance lowers, i_{pv} lowers as well. Consequently, the current reference also lowers as a result, and the error ripple gets smaller, which will increase the switching frequency. An hysteresis band comparator and a Set-Reset Flip-Flop as seen in Fig. 4.4 are used to produce the signal that drives the semiconductor.

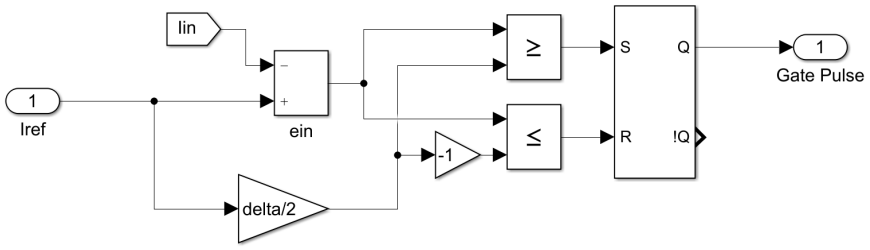

Figure 4.4: Sliding mode current controller.

4.3.2 Linear control

To design the linear controller a mathematical linearized model for the converter must first be derived. Since the converter is non-linear, a method as state-space averaging can be used. This method allows to ignore the non-linear switching dynamics as along as the switching frequency is much higher than the system's critical dynamics (the input capacitor and magnetizing inductance) [23]. The state variables chosen are the PV voltage, v_{pv}, and the current through the magnetizing inductance, i_{Lm}. The equations of the system's dynamics when S_1 is ON are given by (4.34) and (4.35) and expressions (4.36) and (4.37) represent the equations of the system's dynamics when S_1 is OFF:

Equations of the system's dynamics when $\mathbf{S_1}$ is ON:

$$L\frac{di_{Lm}}{dt} = v_{pv} \tag{4.34}$$

$$C_{pv}\frac{dv_{pv}}{dt} = i_{pv} - i_{Lm} \tag{4.35}$$

Equations of the system's dynamics when $\mathbf{S_1}$ is OFF:

$$L\frac{di_{Lm}}{dt} = \frac{v_{pv} - v_{dc}}{n} \tag{4.36}$$

$$C_{pv}\frac{dv_{pv}}{dt} = i_{pv} - \frac{i_{Lm}}{n} \tag{4.37}$$

By averaging (4.34) and (4.36) in regards to the duty-cycle δ, the dynamics of the inductor current is obtained:

$$\frac{di_{Lm}}{dt} = f_1(i_{Lm}, v_{pv}, \delta) =$$
$$= \frac{1}{L_m}\left[v_{pv}\delta + \frac{v_{pv} - v_{dc}}{n}(1-\delta)\right] = \frac{1}{nL_m}\left[v_{pv}(1+\delta(n-1)) - v_{dc}(1-\delta)\right] \tag{4.38}$$

By averaging (4.35) and (4.37) in regards to the duty-cycle δ, the dynamics of the capacitor voltage is obtained:

$$\frac{dv_{pv}}{dt} = f_2(i_{Lm}, v_{pv}, \delta) =$$
$$= \frac{1}{C_{pv}}\left[i_{pv}\delta - i_{Lm}\delta + i_{pv}(1-\delta) - \frac{i_{Lm}}{n}(1-\delta)\right] = \frac{1}{C_{pv}}\left[i_{pv} + \frac{i_{Lm}}{n}(\delta(1-n)-1)\right] \tag{4.39}$$

As expressions (4.38) and (4.39) are still non-linear, a linearization process (4.40) is used to obtain a small signal model around an operation point.

$$\tilde{f} = \left.\frac{\partial f}{\partial v_{pv}}\right|_{SS} \tilde{v_{pv}} + \left.\frac{\partial f}{\partial i_{Lm}}\right|_{SS} \tilde{i_{Lm}} + \left.\frac{\partial f}{\partial \delta}\right|_{SS} \tilde{\delta} \tag{4.40}$$

The small signal models obtained for the inductor current and for the capacitor voltage are obtained in (4.41) and (4.42) respectively.

$$\frac{d\tilde{i_{Lm}}}{dt} = \left.\frac{\partial f_1}{\partial v_{pv}}\right|_{SS} \tilde{v_{pv}} + \left.\frac{\partial f_1}{\partial i_{Lm}}\right|_{SS} \tilde{i_{Lm}} + \left.\frac{\partial f_1}{\partial \delta}\right|_{SS} \tilde{\delta} = \frac{1+\delta_o(n-1)}{nL_m}\tilde{v_{pv}} + \frac{V_{pv_o}(n-1) + V_{dc_o}}{nL_m}\tilde{\delta} \tag{4.41}$$

$$\frac{d\tilde{v_{pv}}}{dt} = \left.\frac{\partial f_2}{\partial v_{pv}}\right|_{SS} \tilde{v_{pv}} + \left.\frac{\partial f_2}{\partial i_{Lm}}\right|_{SS} \tilde{i_{Lm}} + \left.\frac{\partial f_2}{\partial \delta}\right|_{SS} \tilde{\delta} =$$
$$= \frac{\delta_o(1-n)-1}{nC_{pv}}\tilde{i_{Lm}} + \frac{1}{R_{pv}C_{pv}}\tilde{v_{pv}} + \frac{I_{Lm_o}(1-n)}{nC_{pv}}\tilde{\delta} \tag{4.42}$$

The small signal models can be written in the matrix form, as in (4.43).

$$\tilde{f} = \mathbf{A}\tilde{x} + \mathbf{B}\tilde{u} \tag{4.43}$$

From (4.41) and (4.42), the resultant matrix is:

$$\begin{bmatrix} \frac{d\tilde{i_{Lm}}}{dt} \\ \frac{d\tilde{v_{pv}}}{dt} \end{bmatrix} = \begin{bmatrix} 0 & \frac{1+\delta_o(n-1)}{nL_m} \\ \frac{\delta_o(1-n)-1}{nC_{pv}} & \frac{1}{R_{pv}C_{pv}} \end{bmatrix} \begin{bmatrix} \tilde{i_{Lm}} \\ \tilde{v_{pv}} \end{bmatrix} + \begin{bmatrix} \frac{v_{pv_o}(n-1)+v_{dc_o}}{nL_m} \\ \frac{I_{Lm_o}(1-n)}{nC_{pv}} \end{bmatrix} \tilde{\delta} \tag{4.44}$$

The operation point chosen for linearization is during steady-state and with the PV system working at the following conditions: 600 W/m^2 and 45°C cell temperature. This operation point is used instead of the nominal point (NOCT conditions) so that the linear controller works in a wider range of irradiance levels. All the values for this operation point can be observed in table 4.1. By inputting these value into (4.44) matrix (4.45) is obtained.

Table 4.1: Steady-state operation point used for linearization of step-up PPC.

Input voltage V_{pv_o} [V]	28
Output Voltage V_{dc_o} [V]	380
Magnetizing current I_{Lm_o} [A]	9.505
Duty-cycle δ_o [%]	50
Transformer's turn ratio, n	12.57
Magnetizing Inductance L_m [μH]	225
Input Capacitor C_{pv} [μF]	108
PV's dynamic resistance R_{pv} [Ω]	-5.44

$$\begin{bmatrix} \frac{d\tilde{i_{Lm}}}{dt} \\ \frac{d\tilde{v_{pv}}}{dt} \end{bmatrix} = \begin{bmatrix} 0 & 2399 \\ -4907 & -1702 \end{bmatrix} \begin{bmatrix} \tilde{i_{Lm}} \\ \tilde{v_{pv}} \end{bmatrix} + \begin{bmatrix} 248903 \\ -81008 \end{bmatrix} \tilde{\delta} \tag{4.45}$$

To obtain the transfer function for one of the state variable, expression (4.46) is used, where $\tilde{y} = \tilde{i_{Lm}}$ if $C = [1\ 0]$ or $\tilde{y} = \tilde{v_{pv}}$ if $C = [0\ 1]$ and $\tilde{u} = \tilde{\delta}$.

$$\frac{\tilde{y}}{\tilde{u}} = \mathbf{C} \cdot (s\mathbf{I} - \mathbf{A})^{-1} \cdot \mathbf{B} \tag{4.46}$$

Solving for $\tilde{y} = \tilde{v_{pv}}$ the closed-loop transfer function for v_{pv} is obtained:

$$\frac{\tilde{v_{pv}}(s)}{\tilde{\delta}(s)} = \frac{-81008s - 1.22e9}{s^2 + 1702s + 1.18e7} \tag{4.47}$$

A PI controller is then designed to ensure zero error in steady-state. The *MatLab* tool (pidTuner), a graphic method, is used design the controller. The parameters chosen are a damping ratio of ζ = 0.55, initially of 0.707 but reduced to achieve a faster time response, and a cut-off frequency of f_{cf} = 3 kHz, well below the switching frequency of 50 kHz. These resulted in a settling time t_s = 2.56 ms and an overshoot of 20.8%. The obtained designed controller is shown in (4.48) and in table 4.2.

$$C_{v_{pv}}(s) = -0.19205 \cdot \frac{s - 67.2239}{s} \tag{4.48}$$

Table 4.2: PI linear controller parameters.

Proportional gain k_p	-0.19205
Integral gain k_i	-67.2239
Damping ratio ζ	0.55
Cut-off frequency f_{cf}	3 kHz
Settling time	2.56 ms
Overshoot	20.8 %

To prevent the converter from saturating (e.g. due to large disturbances) a limiter is used:

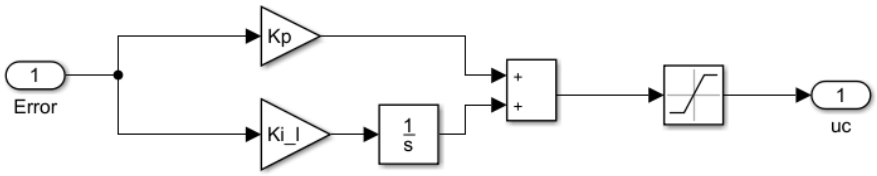

Figure 4.5: Voltage PI controller with limiter.

4.4 Step-down PPC non-linear control

The control design for the step-down PPC is identical to the one used for the step-up PPC. Nonlinear methods as the backstepping technique and sliding mode control are used for the voltage external loop and current internal loop, respectively. Therefore the design of the controller is analogous to the one done for the step-up PPC with some slight differences.

The voltage to be controlled in the step-down PPC is the constant power load voltage, which is the output voltage of the converter (Fig. 2.7). The error e_{Vo} is then defined as:

$$e_{Vo} = V_{Oref} - V_o \tag{4.49}$$

The integral error of the voltage is also defined:

$$e_{I2} = \int_0^t e_{Vo}\,\mathrm{d}t \tag{4.50}$$

As done previously for the step-up PPC controller, the integral error is used to assure zero steady-state error that may occur due to parameters mismatch. Combining the two errors a Lyapunov function is proposed:

$$V_{v2} = K_{I2} \cdot \frac{e_{I2}^2}{2} + \frac{e_{Vo}^2}{2}\ ,\ K_{I2} > 0 \tag{4.51}$$

This function satisfies the conditions in (4.2) for a Lyapunov function and its derivative is:

$$\dot{V}_{v2} = K_{I2} \cdot e_{I2} \cdot \frac{de_{I1}}{dt} + e_{Vo} \cdot \frac{de_{Vo}}{dt} = K_{I2} \cdot e_{I2} \cdot e_{Vo} + e_{Vo} \cdot \frac{de_{Vo}}{dt} \tag{4.52}$$

To guarantee asymptotic stability it must also satisfy (4.3) and so the following constraint is applied :

$$\dot{V}_{v2} < 0 \Rightarrow K_{I2} \cdot e_{I2} \cdot e_{Vo} + e_{Vo} \cdot \frac{de_{Vo}}{dt} = -K_{v2} \cdot e_{Vo}^2 \ , \ K_{v2} > 0 \tag{4.53}$$

In order to apply the backstepping technique the dynamics of the output voltage is used. Since the output voltage is equal to voltage of the output capacitor its derivative can be derived from its current:

$$\frac{dV_o}{dt} = \frac{i_{Co}}{C_o} = \frac{i_o - i_{load}}{C_o} \tag{4.54}$$

Now the derivative of the error e_{Vo} can be determined:

$$\frac{de_{Vo}}{dt} = \frac{dV_{Oref}}{dt} - \frac{i_o - i_{load}}{C_o} \tag{4.55}$$

By using (4.55) in (4.53) and solving for the current i_o the control law for that current is obtained:

$$I_{Oref} = i_{load} + C_o \left(K_{v2} \cdot e_{Vo} + K_{I2} \cdot e_{I2} + \frac{dV_{oref}}{dt} \right) \tag{4.56}$$

This control law is very similar to the one used in the step-up PPC and so a controller as the one in Fig. 4.3 is implemented.

The inner loop controls the output current of the converter using a sliding mode controller. Since the control objective is $i_o = I_{Oref}$ the sliding surface (4.57) of the controller is then the error associated with this current (4.28), which is to be kept in a vicinity of zero.

$$s(i_o) = e_{Io} = I_{Oref} - i_o \tag{4.57}$$

In order to determine the control law for reaching this surface the dynamics of the input current i_o is calculated using (2.24) and (2.33) resulting in (4.58).

$$\frac{di_o}{dt} = \begin{cases} \frac{\frac{di_{L_m}}{dt}}{n} = \frac{v_{dc} - v_o}{n^2 L_m} \ , & \text{if } S_2 \text{ ON} \\ \frac{di_{L_m}}{dt} = \frac{-v_o}{L_m} \ , & \text{if } S_2 \text{ OFF} \end{cases} \tag{4.58}$$

As the DC grid voltage, v_{dc} , is always higher than the output load voltage, v_o , the derivative of the output current has different signs according to the state of the semiconductor switch:

$$\begin{cases} \frac{di_o}{dt} > 0 \Rightarrow \frac{de_{Io}}{dt} < 0 \ , & \text{if } S_2 \text{ ON} \\ \frac{di_o}{dt} < 0 \Rightarrow \frac{de_{Io}}{dt} > 0 \ , & \text{if } S_2 \text{ OFF} \end{cases} \tag{4.59}$$

Knowing this the state of the semiconductor can be chosen in order to satisfy condition (4.3), or in this case $e_{Io} \cdot \frac{de_{Io}}{dt} < 0$:

$$\begin{cases} e_{Io} > 0 \rightarrow \frac{de_{Io}}{dt} < 0 \rightarrow S_2 \text{ ON} \\ e_{Io} < 0 \rightarrow \frac{de_{Io}}{dt} > 0 \rightarrow S_2 \text{ OFF} \end{cases} \tag{4.60}$$

Similarly to the case for the step-up PPC, the step-down PPC also presents discontinuous currents (Fig. 2.8a) and so the error interval must account for the difference between the windings currents. The procedure to determine the difference is the same although in this case the waveforms of the current are different (comparing Fig. 2.4a with Fig. 2.8a). The turns ratio of the transformer is taken into account and considering the boundaries of the error bandwidth it must respect the following condition:

$$\begin{aligned} \frac{I_{Oref} + I_{Oref} \cdot \frac{d}{2}}{n} \leq I_{Oref} - I_{Oref} \cdot \frac{d}{2} \Leftrightarrow \\ \Leftrightarrow d \leq \ 2 \cdot \frac{n-1}{n+1} \end{aligned} \tag{4.61}$$

This time the error approaches the error from outside of the interval instead from within, that's why the error difference condition is now a maximum instead of a minimum. Applying this ratio a maximum error ripple $\Delta_{\text{max}} = I_{Oref} \cdot d$ is obtained. This ripple is then decreased $\Delta = \Delta_{\text{max}} - \Delta_{\text{add}}$ to match the desired switching frequency, in this case 100 kHz. Finally the control law (4.62) is obtained replacing zero with the error interval in (4.60):

$$\begin{cases} e_{Io} > \frac{\Delta}{2} \rightarrow \frac{de_{Io}}{dt} < 0 \rightarrow S_2 \text{ ON} \\ e_{Io} < -\frac{\Delta}{2} \rightarrow \frac{de_{Io}}{dt} > 0 \rightarrow S_2 \text{ OFF} \end{cases} \tag{4.62}$$

An hysteresis band comparator and a Set-Reset Flip-Flop are used, similarly to the one in Fig. 4.4, to produce the signal that drives the semiconductor.

4.5 DAB non-linear control

Unlike the previous controllers, the one designed for the DAB converter uses only the backstepping technique and focuses on the control strategy presented in [15].

A non-linear approach to control of the DAB converter is beneficial since there will be CPLs connected to the DC microgrid and these can affect the stability of the grid. As the power consumed by these loads is constant it means the derivative of P_{OUT} is zero:

$$P_{OUT} = V_{DC} \cdot I_g = constant \Rightarrow dP_{OUT} = 0 \tag{4.63}$$

This results in a negative incremental resistance:

$$dP_{OUT} = V_{DC} \cdot dI_G + dV_{DC} \cdot I_G = 0 \Leftrightarrow \frac{dV_{DC}}{dI_G} = -\frac{V_{DC}}{I_G} = -r_i \tag{4.64}$$

A negative resistance can result in oscillatory voltage since a decrease in input voltage means an increase in input current, leading to an higher voltage reduction. The use of the backstepping technique which relies on Lyapunov stability theory is able to lead the DC microgrid voltage to an equilibrium point.

The DAB converter is responsible for setting the DC microgrid voltage and so the control objective is $V_{DC} = V_{DCref}$. The error associated with V_{DC} is then defined as:

$$e_{Vdc} = V_{DC} - V_{DCref} \tag{4.65}$$

The following Lyapunov function is used:

$$V_{v3} = \frac{1}{2} e_{Vdc}^2 \tag{4.66}$$

Which derivative must satisfy condition (4.3):

$$\dot{V}_{v3} = e_{Vdc} \cdot \dot{e}_{Vdc} < 0 \tag{4.67}$$

In order to do so the following constraint is applied:

$$e_{Vdc} \cdot \dot{e}_{Vdc} = -K_{v3} \cdot e_{Vdc}^2 \Leftrightarrow \frac{de_{Vdc}}{dt} = -K_{v3} \cdot e_{Vdc} \ , \ K_{v3} > 0 \tag{4.68}$$

Where K_{v3} is greater than zero. Equation (4.69) is obtained using (4.65) in (4.68):

$$\frac{dV_{DCref}}{dt} - \frac{dV_{DC}}{dt} = -K_{v3} \cdot e_{Vdc} \tag{4.69}$$

By taking into account the dynamics of the DAB converter capacitor voltage (4.70) a control law for the current reference I_{DCref} is obtained:

$$\frac{dV_{DC}}{dt} = \frac{I_{DC} - I_g}{C_g} \tag{4.70}$$

$$I_{DCref} = C_g \frac{dV_{DCref}}{dt} + C_g \cdot K_{v3} \cdot e_{Vdc} + I_g \tag{4.71}$$

If $I_{DC} = I_{DCref}$ then the error e_{Vdc} converges asymptotically to zero. However I_{DC} is not a state variable so its average value I_{DCav} taken over a switching period T_s is used instead. A new error can be defined:

$$e_{Idc} = I_{DCref} - I_{DCav} \tag{4.72}$$

The integral of this error is taken and must be zero in order to make $I_{DCav} = I_{DCref}$. The integral of the error is defined as:

$$e_{I3} = \int_0^t e_{Idc} \, \mathrm{d}t \tag{4.73}$$

Once again a Lyapunov function is defined:

$$V_{I3} = \frac{1}{2} e_{I3}^2 \tag{4.74}$$

And to satisfy $\dot{V}_{I3} < 0$ as per condition (4.3):

$$\frac{de_{I3}}{dt} = -K_{I3} \cdot e_{I3} \ , \ K_{i3} > 0 \tag{4.75}$$

Where K_{I3} is higher than zero for stability. Finally the control law for the I_{DCav} is obtained by using (4.71) and (4.73) in (4.75):

$$I_{DCav} = C_g \frac{dV_{DCref}}{dt} + C_g \cdot K_{v3} \cdot e_{Vdc} + I_g + K_{I3} \cdot e_{I3} \tag{4.76}$$

As was explained in section 2.4 the control input for the DAB converter is not the current I_{DC} and instead it is the phase shift φ between the full-bridge square voltages v_{s1} and v_{s2}. If we assume that V_{DC} is constant we can use $V_{DC}I_{DC} = \eta P_{DAB}$, where P_{DAB} is taken from (2.42), to obtain an expression relating I_{DC} with φ:

$$I_{DCav} = G\frac{\varphi}{\pi}(\pi - \varphi) \tag{4.77}$$

Where $G = \frac{nV_p\eta}{2\pi f L}$. Equation (4.77) is solved for the phase shift φ:

$$\varphi = \frac{\pi}{2} \pm \frac{\pi}{2}\sqrt{1 - 4\frac{I_{DCav}}{G\pi}} \tag{4.78}$$

The phase shift value calculated through this expression guarantees $V_{DC} = V_{DCref}$. In Fig. 4.6 the implemented controller is shown. The f block corresponds to equation (4.78).

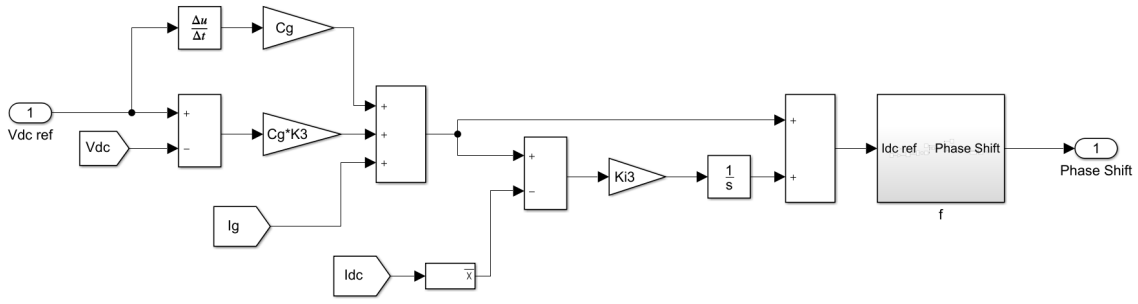

Figure 4.6: Backstepping controller for the DAB converter.

Chapter 5

Obtained results

The operation of the sized converters and designed controllers will be analyzed in order to evaluate their performance. Using *MatLab/Simulink* the elements in Fig. 2.1 were modelled and tested in different operation scenarios:

- Scenario 1 - Stand-alone operation of PV panel in nominal conditions
- Scenario 2 - Stand-alone operation of PV panel with irradiance levels change
- Scenario 3 - Stand-alone operation of constant power loads
- Scenario 4 - DC grid behaviour when both PV panel and CPLs are connected and disconnected

5.1 Scenario 1 - PV panel operation in nominal conditions

The first scenario tested focuses on the PV system working at nominal conditions which are an irradiance of 800 W/m^2 and a cell temperature of 45 $C°$, previously described as NOCT conditions. In these conditions the panel operates at its MPP, if its voltage is 28V and is supplying a power of around 188W [18]. The connection of the PV system is made using the step-up PPC and its simulation parameters are the same ones presented in table 2.1. In Fig. 5.1 the *MatLab/Simulink* model used to test scenario 1 and 2 is shown. Only the step-up PPC and DAB converter are included since only the PV system is connected to the DC microgrid.

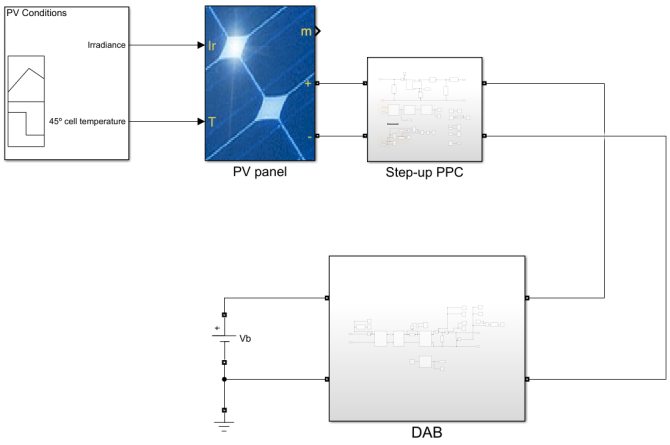

Figure 5.1: *MatLab/Simulink* model used for scenario 1 and 2.

In Fig. 5.2 both the PV voltage and MPPT voltage reference are shown as results from using the controllers designed in section 4.1 (MPPT algorithm) and 4.3 (step-up PPC control). In this figure the comparison between the nonlinear controller (Fig. 5.2a) and linear controller (Fig. 5.2b), designed in the previous section for the step-up PPC, can also be observed. It is clear in both cases that the PV voltage has reached the desired MPP of 28V and it is oscillating around this value, as is expected from the P&O method. Both controllers are able to make the PV voltage follow the MPPT voltage reference for a MPPT period of 5 ms with similar results. The linear controller has a slightly higher response time and the voltage takes a little longer to stabilize around the reference with this MPPT period, but the difference is minimal.

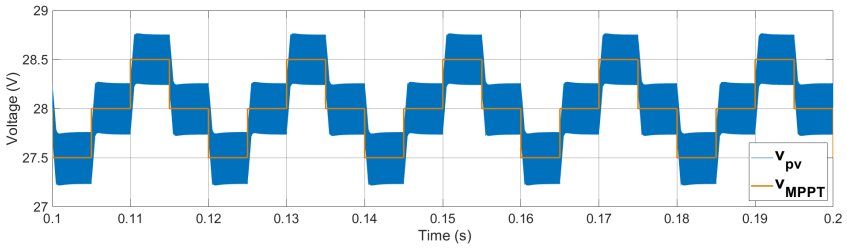

(a) Non-linear controller - PV voltage v_{pv} (blue) and MPPT reference voltage v_{MPPT} (orange).

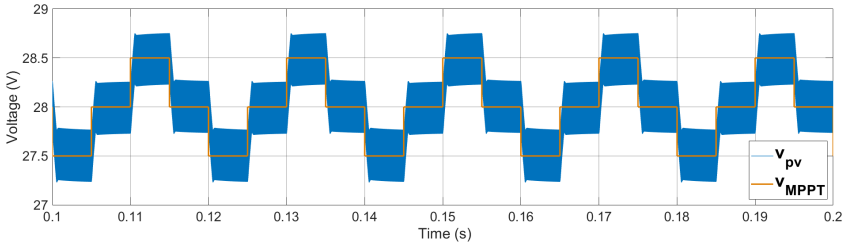

(b) Linear Controller - PV voltage v_{pv} (blue) and MPPT reference voltage v_{MPPT} (orange).

Figure 5.2: Comparison of voltage MPPT tracking of a non-linear controller and linear controller during nominal operation.

Furthermore, the power generated by the PV panel is seen in Fig. 5.3. It is slightly above 188W, around 191W, and this may be due to a mismatch between the actual values from the PV panel datasheet and the ones used in the *Simulink* model. Nonetheless the values are close enough to conclude that it is working correctly. It can be noted that the slight oscillation observed in the power is due to the voltage level being constantly oscillating around 28V. The partial power ratio K_{pr} also presents this oscillation (Fig. 5.4) but matches the expected value, averaging at $K_{pr} \approx 0.9265$, very close to the 0.9263 theoretical value.

A comparison of losses between the step-up PPC and the flyback converter is also made because of their similarities. Conduction losses are accounted for all of the converters elements and so are the switching losses for the MOSFET semiconductor. It must be noted that the *Simulink* model of the semiconductors is ideal, so a parallel RC circuit is added to simulate switching losses, sized for a turn-on and turn-off time of 100 ns. The flyback converter that is used as comparison is sized to work at the same conditions as the step-up PPC. In table 5.1 the parameters used to model the conduction

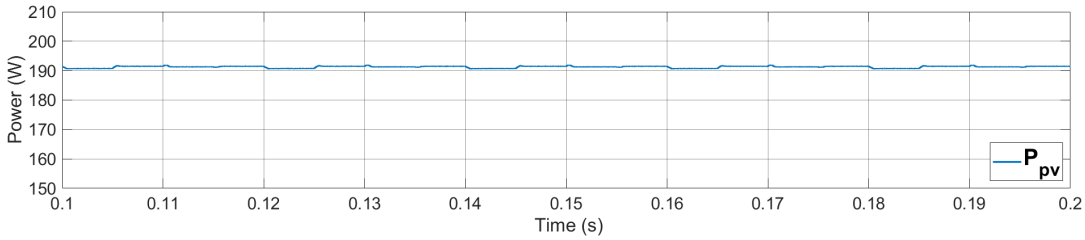

Figure 5.3: Input PV power P_{pv}.

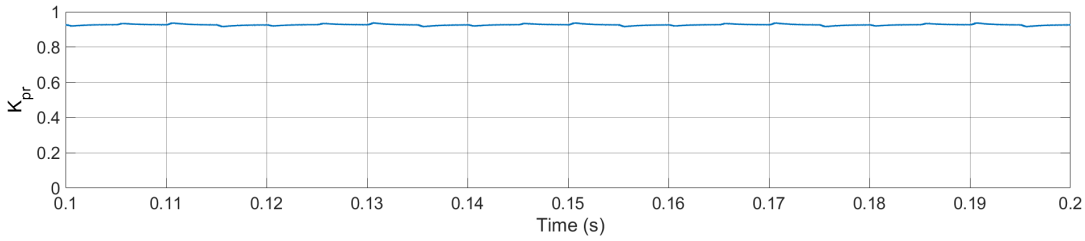

Figure 5.4: Partial power ratio K_{pr} of the step-up PPC during nominal operation.

losses are displayed. Except for the transformer's winding resistances and input capacitor resistance, which are sized for 0.5% of the input power in losses, all the parameters were taken from datasheets of components appropriate to work at the voltages and currents of the system at nominal operation. The transformer of the step-up PPC was also sized for a fraction of the input power, equal to the partial power ratio $K_{pr} = 0.9263$, effectively reducing the conduction losses.

Table 5.1: Non ideal elements used to model conduction losses in both converters.

Step-up PPC primary winding resistance R_1 [$m\Omega$]	10
Flyback primary winding resistance R_{1fb} [$m\Omega$]	11
Step-up PPC secondary winding resistance R_2 [$m\Omega$]	126
Flyback secondary winding resistance R_{2fb} [$m\Omega$]	150
Input capacitor resistance R_c [$m\Omega$]	30
Mosfet ON resistance R_{ds} [$m\Omega$]	17
Diode resistance R_d [$m\Omega$]	21.5
Diode forward voltage V_d [V]	0.9

The MPPT algorithm is turned off for this comparison of losses and instead the non-linear voltage controller is given a constant voltage reference of 28V. This will eliminate the oscillation of the voltage value around 28V and make it easier to compare the values between the converters. For each converter (step-up PPC and flyback) the power being generated by the PV system is measured as well as the output power, then the efficiency of the converter is computed. The results are seen in Fig. 5.5 and Fig. 5.6 for the step-up PPC and Flyback converter, respectively.

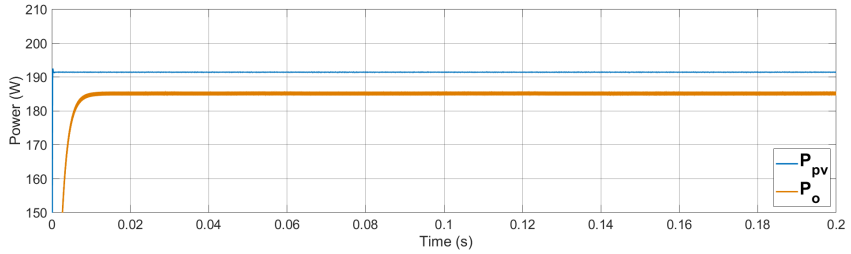

(a) Input PV power P_{pv} (blue) and output power P_o (orange).

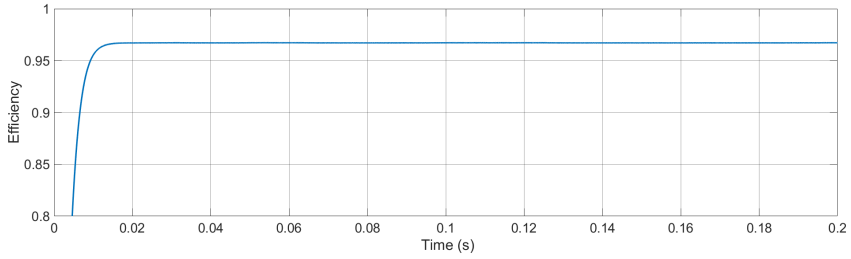

(b) Efficiency.

Figure 5.5: Input power, output power and efficiency for nominal operation of the step-up PPC considering conduction and switching losses.

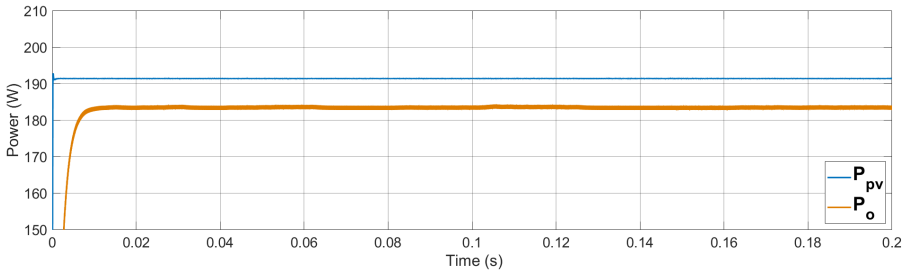

(a) Input PV power P_{pv} (blue) and output power P_o (orange).

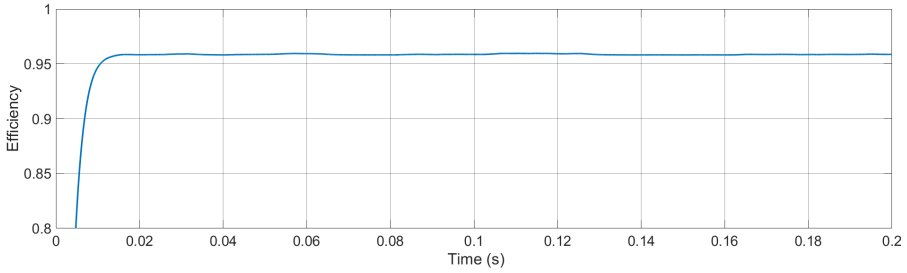

(b) Efficiency.

Figure 5.6: Input power, output power and efficiency for nominal operation of the Flyback converter considering conduction and switching losses.

While in both cases the input power was the same, $P_{pv} = 191.6W$, the output power differed. The step-up PPC reached an output power of $P_o = 185.2W$ and efficiency of $\eta = 96.7\%$ whereas the flyback converter reached an output power of $P_o = 183.6W$ and efficiency of $\eta = 95.8\%$. The voltage and currents in the semiconductors also differ. The K_{pr} also slightly increased in the step-up PPC when losses were simulated because it depends on the efficiency of the converter and it was previously simulated without considering them. Table 5.2 summarizes the differences between the converters, including the voltage and current levels in the semiconductors. In comparison to the flyback converter the step-up PPC is able to achieve a better efficiency while also reducing the semiconductors ratings.

Table 5.2: Differences between step-up PPC and flyback at nominal operation.

Parameter	Step-up PPC	Flyback
Input power [W]	191.6	191.6
Output power [W]	185.2	183.6
Efficiency [%]	96.7	95.8
MOSFET blocking voltage [V]	56	56
MOSFET drain current [A]	6.35	6.83
Diode blocking voltage [V]	700	756
Diode forward current [A]	0.48	0.48

5.2 Scenario 2 - PV panel operation with irradiance levels change

The second scenario is still focused in the PV system, however in this case the irradiance levels change during the simulation in order to evaluate if the system is able to respond to these changes, namely if the PV panel maintains its MPP operation. The *MatLab/Simulink* model for this scenario is the one seen in Fig. 5.1, since the focus is still in the connection of the PV system to the DC microgrid. A comparison between the nonlinear and linear controllers for the step-up PPC is also made in this scenario.

The irradiance levels change in the following order:

- Instant t = $0s$: Irradiance = 600 W/m^2
- Instant t = $0.2s$: Irradiance = 800 W/m^2
- Instant t = $0.4s$: Irradiance = 400 W/m^2
- Instant t = $0.6s$: Irradiance = 200 W/m^2

Each irradiance level lasts for 0.2s for a total test duration of 0.8s. The cell temperature is kept at 45 C° and so the MPP voltage shouldn't deviate much from 28V (Fig. 3.3) even though the irradiance levels change. In Fig. 5.7a the results for using the nonlinear controller are presented. The controller is able to maintain the MPPT for all irradiances. The voltage reference, v_{MPPT}, oscillates around the value of 28V for all irradiance levels except the last one of 200 W/m^2 where it dropped to 27.5V. Although not as significant as the cell temperature this voltage drop is expected since a decrease of irradiance slightly decreases the MPP voltage.

The linear controller showed a similar performance to the nonlinear controller, following the voltage MPPT reference and oscillating around the value of 28V for all irradiance levels except for the one of 200 W/m^2 in which it also dropped to the value of 27.5V. Since the linear controller is designed to operate at 600 W/m^2 and at 45 C°, it is expected that its behaviour worsens the further away the PV system is working from that operation point. That is the case for the operation at 200 W/m^2, shown in Fig. 5.8b where the transient behaviour of the voltage is showing more oscillation than in operation points with

higher irradiance levels. On the other hand the nonlinear controller performance is not affected by the irradiance level even though the switching frequency changes according to the irradiance level.

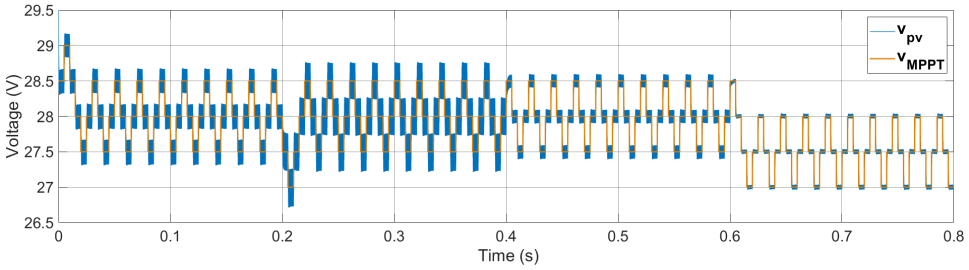

(a) Non-linear controller - PV voltage v_{pv} (blue) and MPPT reference voltage v_{MPPT} (orange).

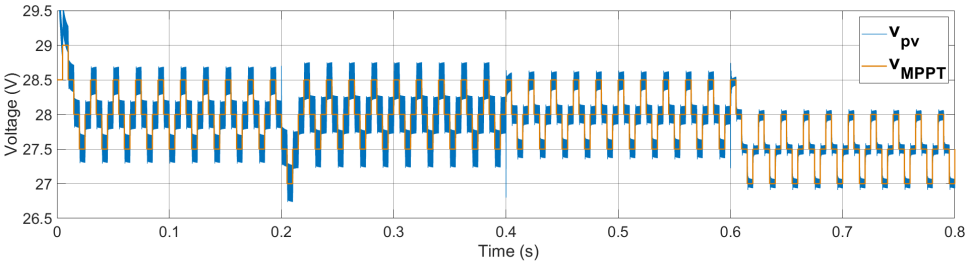

(b) Linear controller - PV voltage v_{pv} (blue) and MPPT reference voltage v_{MPPT} (orange).

Figure 5.7: Comparison of voltage MPPT tracking of a non-linear controller and linear controller for various irradiance levels.

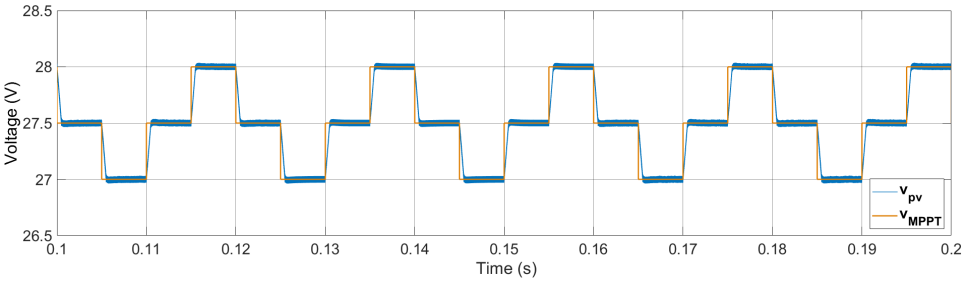

(a) Non-linear controller - PV voltage v_{pv} (blue) and MPPT reference voltage v_{MPPT} (orange).

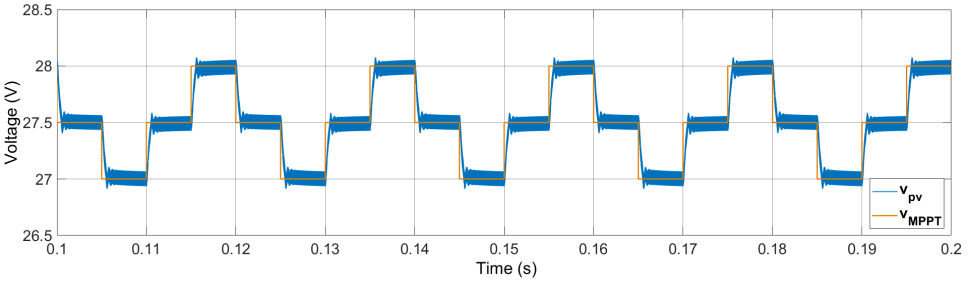

(b) Linear controller - PV voltage v_{pv} (blue) and MPPT reference voltage v_{MPPT} (orange).

Figure 5.8: Comparison of voltage MPPT tracking of a non-linear controller and linear controller at a 200 W/m^2 irradiance level.

Figures 5.9 and 5.10 show the power generated by the PV system and the partial power ratio respectively, for the various irradiance levels while using the nonlinear controller. The results are as expected, with the power generated by the PV system being proportional to the irradiance level and the partial

power ratio of the step-up PPC remaining mostly constant (besides the disturbances that occur when the irradiance is changed). The partial power ratio should remain constant for the different irradiances since it depends on the voltage gain of the converter, which remains the same for all the irradiances except for the last one of 200 W/m^2.

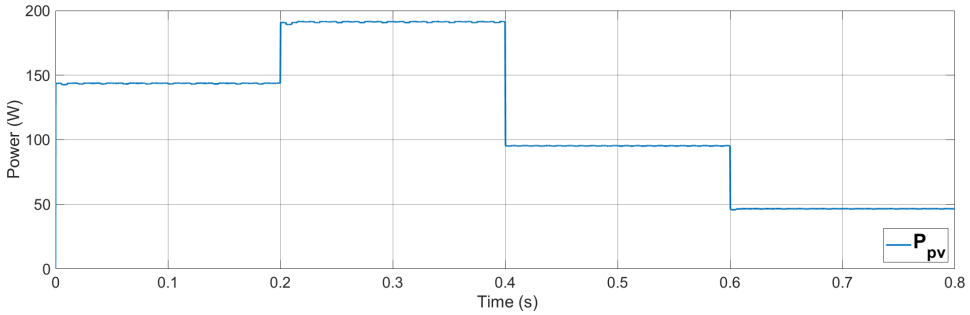

Figure 5.9: Input PV power P_{pv} for the various irradiance levels.

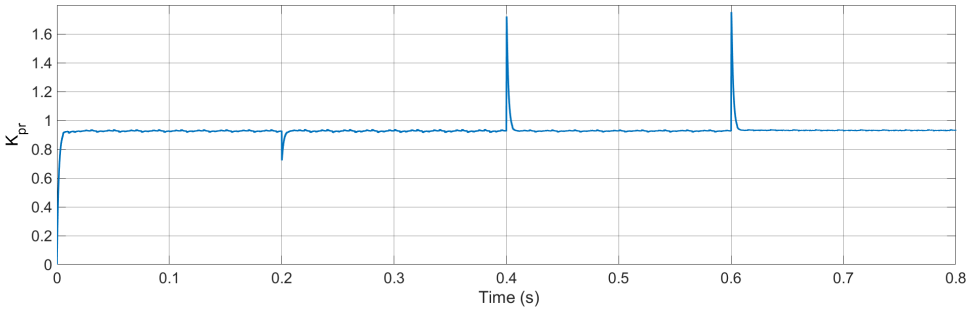

Figure 5.10: Partial power ratio K_pr of the step-up PPC for various irradiance levels.

Table 5.3 compiles the results of this scenario while using the nonlinear controller. The switching frequency is also measured since it changes according to the irradiance level, as explained in section 4.3.1. The switching frequency is 50 kHz for the 800 W/m^2 and it increases up to 112 kHz at 200 W/m^2, so even though the nonlinear controller is able to follow the voltage reference in low irradiance conditions, the converter is working at a switching frequency higher than the one the converter was designed for.

Table 5.3: Results for the scenario 2 test using the nonlinear controller.

Irradiance [W/m^2]	800	600	400	200
MPP voltage [V]	28	28	28	27.5
Input PV power P_{pv} [W]	191	144	95	47
Partial power ratio K_{pr} [%]	92.6	92.6	92.6	92.6
Switching frequency f_s [kHz]	50	57	70	112

5.3 Scenario 3 - Stand-alone operation of constant power loads

The stand-alone operation of the step-down PPC is tested in the third scenario and its simulation parameters are the same ones in table 2.2. The two constant power loads tested are the 300W/48V load and the 200W/24V load. The *MatLab/Simulink* model used for this scenario is shown in Fig. 5.11 where only the step-down PPC and the DAB converter are included since this scenarios focuses on the connection of the constant power loads. The step-down PPC is connected to the 380V DC microgrid at instant $t = 0s$ and the test runs for 0.4s. The output voltage, output power and partial power ratio for each load are measured and compared.

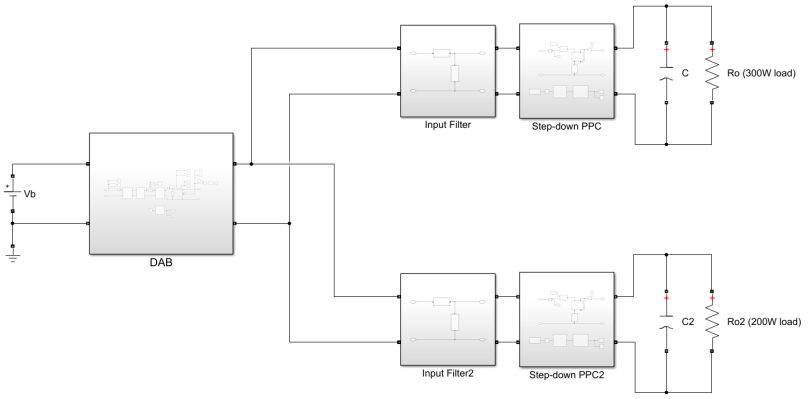

Figure 5.11: *MatLab/Simulink* model used for scenario 3.

After the PPC is connected to the DC microgrid a soft-starter is used to linearly increase the voltage reference from 0V to the desired load voltage and the final values are reached after 0.01s (Fig. 5.12). The soft-starter reduces the disturbances in the DC microgrid.

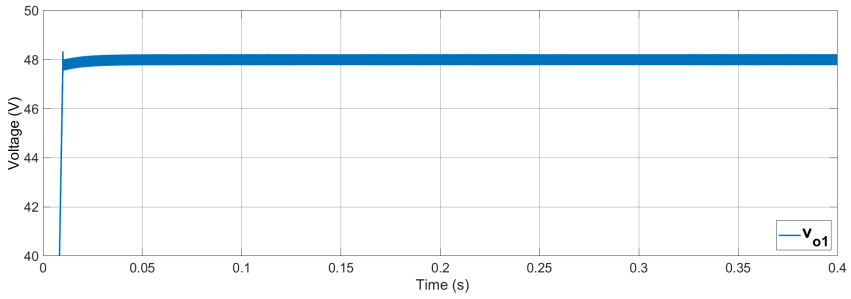

(a) Output voltage v_{o1} for the 48V load.

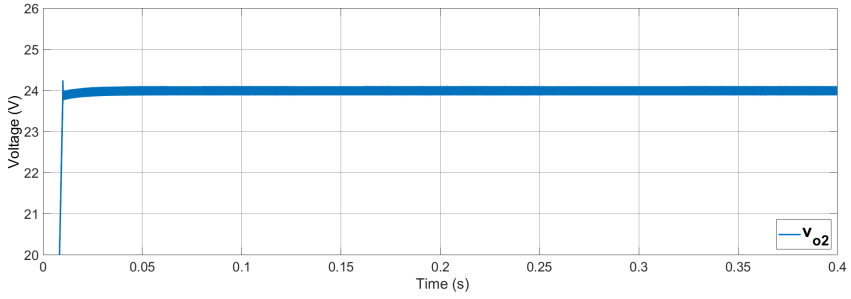

(b) Output voltage v_{o2} for the 24V load.

Figure 5.12: Output voltage for each of the constant power loads.

After 0.01s the power consumed by the constant power load also reaches the desired values (Fig. 5.13). The step-down PPC behaved similarly for both loads, achieving an output voltage of 48V for the first load, an output voltage of 24V for the second load and maintaining the maximum voltage ripple at a maximum of 1%.

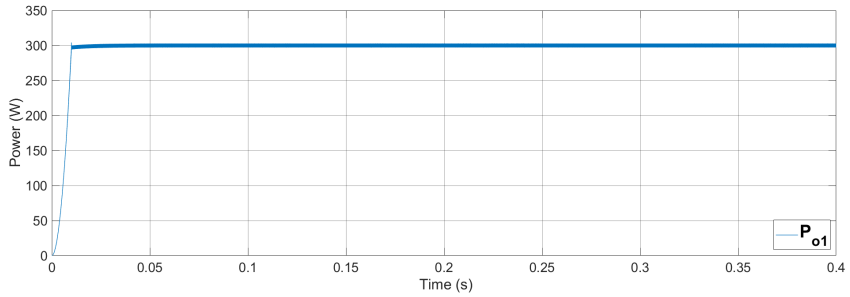

(a) Output power P_{o1} for the 48V load.

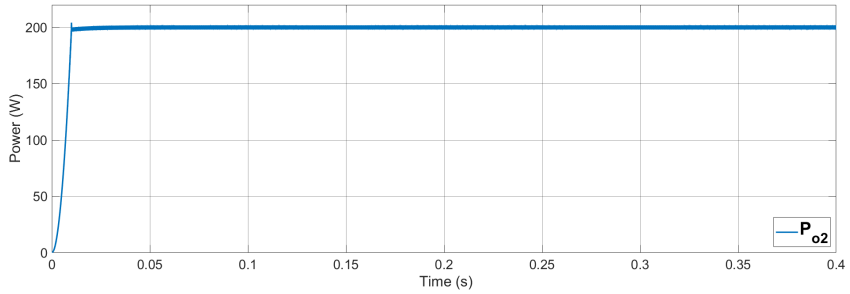

(b) Output power P_{o2} for the 24V load.

Figure 5.13: Output power for each of the constant power loads.

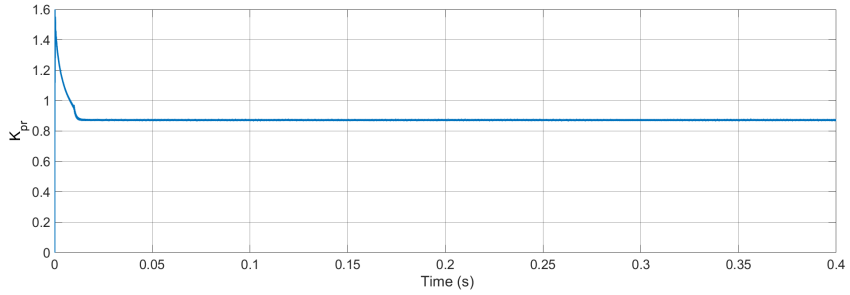

(a) Partial power ratio K_{pr} of the step-down PPC for the 48V load.

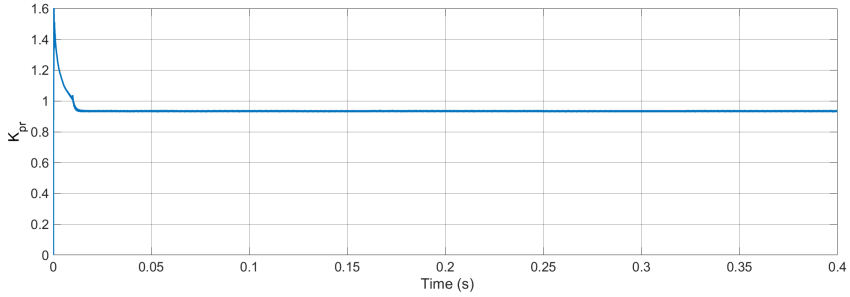

(b) Partial power ratio K_{pr} of the step-down PPC for the 24V load.

Figure 5.14: Partial power ratio of the step-down PPC for each of the constant power loads.

As expected the results for the partial power ratio differed (Fig 5.14). Since the voltage gain is different for the two loads tested so will be the partial power ratio, as is expressed in (2.28). The 24V load presents a smaller voltage gain $G_{v_{PPC}} = \frac{v_o}{v_{dc}}$ than the 48V load, thus the expected K_{pr} is higher (table 2.2).

Both results are close to the theoretical value: the partial power ratio achieved by the step-down PPC connected to the 48V load is of $K_{pr} = 0.872$, while the partial power ratio of the PPC connected to the 24V load is $K_{pr} = 0.9365$. Taking into account the partial power definition of the step-down PPC (2.28) the 48V load achieved a better partial power ratio because its voltage is higher and closer to the DC microgrid voltage than the 24V load.

5.4 Scenario 4 - DC grid behaviour when both PV panel and CPLs are connected and disconnected

The fourth and last scenario is aimed at observing the DC microgrid behaviour, namely its voltage and current, when both the PV system and CPLs are connected, disconnected or working simultaneously. This scenario includes all of the DC microgrid elements as can be seen in Fig. 5.15. The simulation parameters for the DAB converter are the same ones presented in table 2.4.

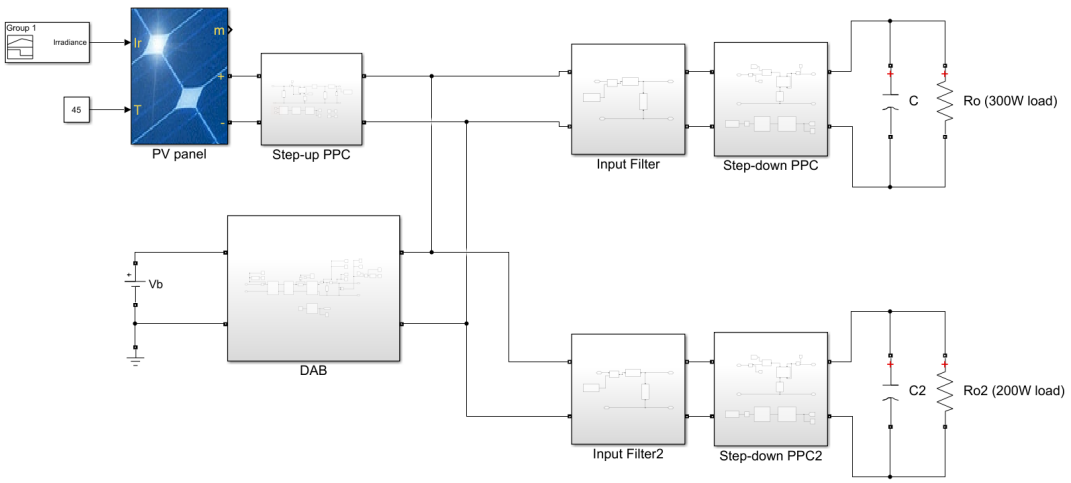

Figure 5.15: *MatLab/Simulink* model used for scenario 4.

As the DAB converter is responsible for setting and maintaining the DC microgrid voltage v_{dc} and balancing the power flow, its output current i_g is indicative if the DAB converter is either consuming or generating power. A negative value of i_g means power is being consumed while a positive value means the DAB is generating power.

The test has a duration of 0.3s and consists of the following steps:

- Instant $t = 0s$: PV system is connected at NOCT conditions: 800 W/m^2 and 45 C° cell temperature
- Instant $t = 0.1s$: 200W/24V load is connected
- Instant $t = 0.2s$: PV system is disconnected and 300W/48V load is connected

The test consists of three periods where the power processed by the DAB converter is different. Until $t = 0.1s$ only the PV system is connected and so the DAB converter must consume all of its power (current i_g must be negative). From $t = 0.1s$ until $t = 0.2s$ both the PV system and 200W load are connected and since the PV system generates almost 200W in NOCT conditions the DAB converter will work at low power (current i_g must be close to zero). Finally, at $t = 0.2s$ the PV system is disconnected and the 300W load is connected. This amounts to a total power being consumed of 500W (current i_g should be positive).

In Fig. 5.16 the voltage and current at the output of DAB converter can be seen. Except for a small dip after connecting the 300W load the output voltage remained close to the value of 380V for the duration of the test. On the other hand, the current presents two spikes which are caused by the charging of the input filters of the step-down PPCs when they are connected at $t = 0.1s$ and $t = 0.2s$.

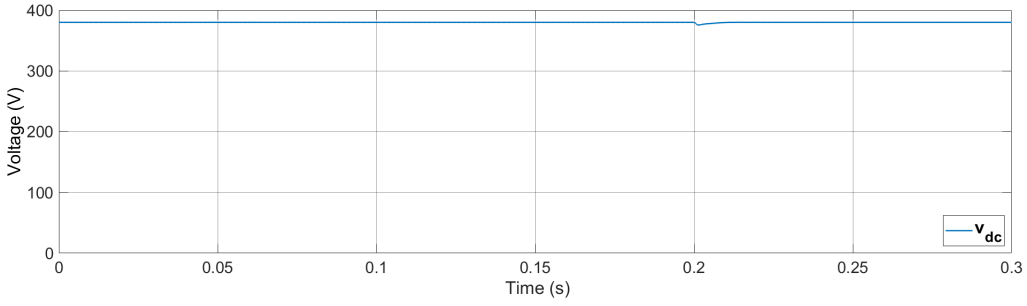

(a) DC microgrid voltage v_{dc}.

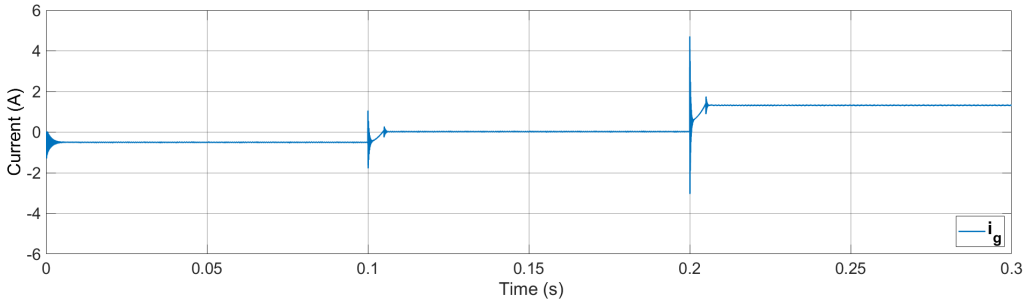

(b) DAB converter output current i_g.

Figure 5.16: DC microgrid voltage and current during scenario 4 test.

Observing Fig. 5.16 and Fig. 5.17 confirms that the DAB converter is working correctly in the three different zones. First it consumes around 190W and its current is negative, in the following zone both its power and current are close to zero because the PV system power closely matches the load's power and lastly the DAB generates 500W and its current is positive.

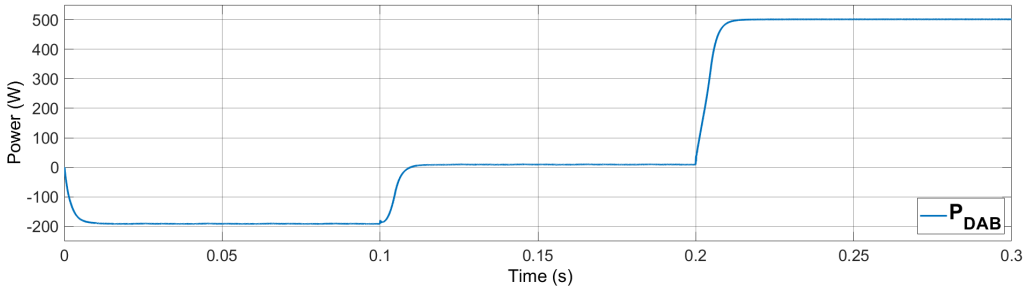

Figure 5.17: Power being processed by the DAB converter.

The voltages of the PV system and the loads are presented in Fig. 5.18, where the MPPT can be seen working in the PV voltage as well as the soft-starters for the step-down PPCs.

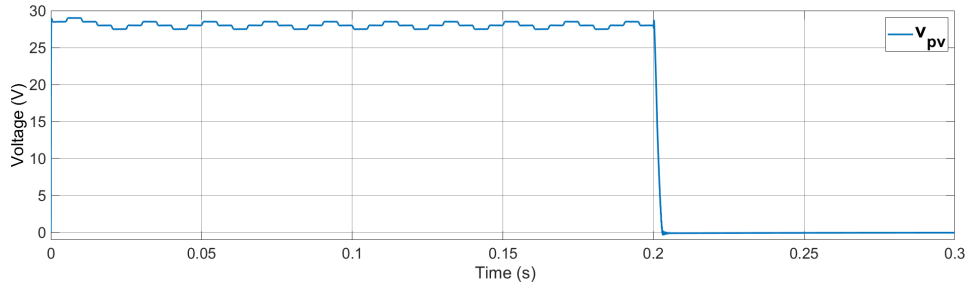

(a) PV voltage v_{pv}.

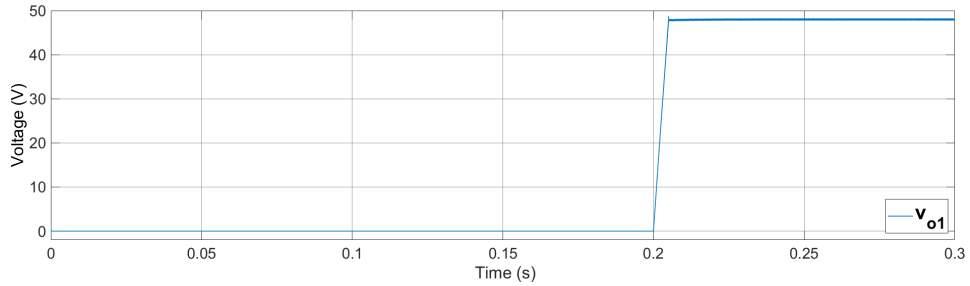

(b) Output voltage v_{o1} for the 48V load.

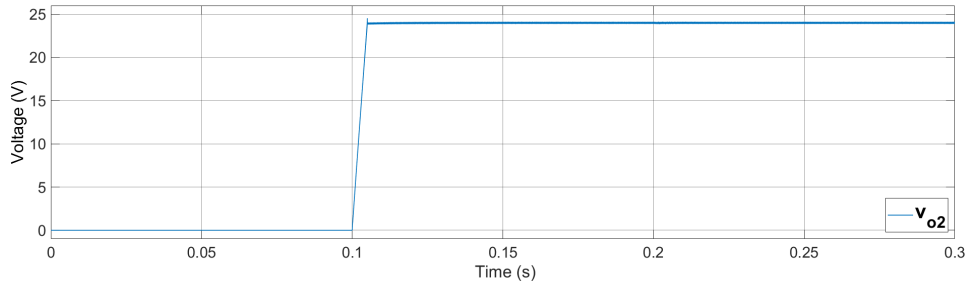

(c) Output voltage v_{o2} for the 24V load.

Figure 5.18: PV voltage and load output voltages during scenario 4 test.

The DAB converter proved to be a suitable converter guaranteeing bidirectional power flow. Due to the non-linear controllers the DC microgrid robustness to changes in operating conditions is achieved, maintaining the DC microgrid voltage stable while both generation of power and consumption occurred. Additionally, the results of this scenario show that all the elements of the DC microgrid are sized appropriately and the desired behaviour of the DC microgrid is achieved.

Chapter 6

Conclusions

In this chapter the conclusions taken from this dissertation are presented as well as suggestions for future work.

6.1 Final Conclusions

The main objective of this thesis was to study a converter topology, based on the technique of partial power processing, in the context of a DC grid and analyze if its performance presents benefits over existing converters, namely a better efficiency and a reduction in the power ratings of the converter's components. This converter topology was originally proposed as the DC-DC stage of the connection of a PV system to an AC grid, but in the case of connection to a DC grid its use is even more justified since no AC-DC stage is needed. Furthermore, it is possible to modify the direction of the power flow of the partial power converter and use it to connect constant power loads to the DC grid.

A DC microgrid was designed in order to study the proposed converter and so the following elements were designed and sized: the first one was the partial power converter working as a step-up converter for the connection of a PV panel to the microgrid. The second converter used a similar topology to the previous one but was modified in order to work as step-down converter and connect a constant power load to the microgrid. Finally a converter able to set the voltage and balance the power flow in the DC microgrid is chosen and sized. Besides these three main elements, filters were also designed for the step-up and step-down converter.

All of these elements needed a control strategy. In the case of the PV system an MPPT algorithm was implemented to guarantee that it was always working at its maximum power for any given operating condition. In the case of the converters non-linear controllers were adopted: these were based on Lyapunov's stability theory and applied the backstepping technique and sliding mode control. For the case of the step-up PPC a classic linear controller was also designed for comparison purposes.

The DC microgrid was modelled and simulated in *Matlab/Simulink* where various scenarios were tested. The scenarios focused on analyzing both particular elements of the DC microgrid as well as the DC microgrid overall. The obtained results were satisfactory and were the expected ones: the MPPT algorithm was able to guarantee maximum power generation from the PV panel for any irradiance level; the step-

up PPC connected the PV panel to the DC microgrid while obtaining a better efficiency and lower power ratings for its components in comparison to the similar and commonly used flyback converter; the step-down PPC was able to connect two different voltage level loads to the DC microgrid while being able to process less power than what it was delivering; the DAB converter was able to balance the difference between power generation and consumption in different conditions while maintaining the DC microgrid voltage stable; the non-linear controllers were shown to have a fast response and able to easily attenuate oscillations.

Concluding, it can be said that the converters and controllers were well sized for functioning in a DC grid and it became apparent that the use of this partial power converter topology offers advantages such as flexibility by working either as step-up or step-down converter, improving efficiency over more commonly used converters and reducing power ratings of components used and therefore associated costs.

6.2 Future Work

In the prospect of continuing the work developed in this Master Thesis the main suggestion is to conduct experimental tests in a laboratory setting. In a first phase, one converter is enough since it can be easily modified to work either as a step-up or step-down converter allowing for the testing of both without acquiring more than one. In a later stage it would be interesting to model the DC microgrid in laboratory settings through the use of more than one partial power converter, a PV system and a bidirectional converter.

Other suggestions include testing this topology for different voltage levels, or in other words for different voltage gains. The power processed by the PPC depends on this voltage gain and so this test could reveal how much further the efficiency and power ratings can be improved. Another suggestion would be to test other partial power processing topologies, for example one suitable for higher power conditions since this one was limited by the flyback transformer.

Bibliography

[1] M. Kasper, D. Bortis, and J. W. Kolar, "Classification and comparative evaluation of PV panel-integrated DC-DC converter concepts", *IEEE Transactions on Power Electronics*, vol. 29, no. 5, pp. 2511-2526, May 2014.

[2] R. M. Button, "An advanced photovoltaic array regulator module", *IECEC 96. Proceedings of the 31st Intersociety Energy Conversion Engineering Conference*, vol. 1, pp. 519-524, 1996.

[3] J. W. Zapata, S. Kouro, G. Carrasco, H. Renaudineau, and T. A. Meynard, "Analysis of partial power DC-DC converters for two-stage photovoltaic systems", *IEEE Journal of Emerging and Selected Topics in Power Electronics*, vol. 7, no. 1, pp. 591-603, 2019.

[4] J. Anzola, I. Aizpuru, A. A. Romero, A. A. Loiti, R. Lopez-Erauskin, J. S. Artal-Sevil, and C. Bernal, "Review of architectures based on partial power processing for DC-DC applications", *IEEE Access*, vol. 8, pp. 103405-103418, 2020.

[5] S. Muller, M. Deicke, and R. W. De Doncker, "Doubly fed induction generator systems for wind turbines", *IEEE Industry Applications Magazine*, vol. 8, no. 3, pp. 26-33, May 2002.

[6] A. G. Birchenough, "A high efficiency DC bus regulator / RPC for spacecraft applications", *AIP conference proceedings*, vol. 699, pp. 606-613, 2004.

[7] M. S. Agamy, M. Harfman-Todorovic, A. Elasser, S. Chi, R. L. Steigerwald, J. A. Sabate, A. J. McCann, L. Zhang, and F. J. Mueller, "An efficient partial power processing DC/DC converter for distributed PV architectures", *IEEE Transactions on Power Electronics*, vol. 29, no. 2, pp. 674-686, February 2014.

[8] J. W. Zapata, H. Renaudineau, S. Kouro, M. A. Perez, and T. A. Meynard, "Partial power DC-DC converter for photovoltaic microinverters", *IECON 2016 - 42nd Annual Conference of the IEEE Industrial Electronics Society*, pp. 6740-6745, 2016.

[9] E. Rodríguez-Díaz, F. Chen, J. Vasquez, J. Guerrero, R. Burgos, and D. Boroyevich, "Voltage-Level selection of future two-level LVdc distribution grids: A compromise between grid compatibiliy, safety, and efficiency", *IEEE Electrification Magazine*, vol. 4, pp. 20-28, 2016.

[10] *SolarPower Europe*, "Global market outlook for solar power 2019 - 2023", Online, 2019, Available: https://www.solarpowereurope.org/wp-content/uploads/2019/05/SolarPower-Europe-Global-Market-Outlook-2019-2023.pdf.

[11] M. Albach, T. Durbaum, and A. Brockmeyer, "Calculating core losses in transformers for arbitrary magnetizing currents a comparison of different approaches", *PESC Record. 27th Annual IEEE Power Electronics Specialists Conference*, vol. 2, pp. 1463-1468, 1996.

[12] Xiangjun Zhang, Hankui Liu, and Dianguo Xu, "Analysis and design of the flyback transformer", *IECON'03. 29th Annual Conference of the IEEE Industrial Electronics Society (IEEE Cat. No.03CH37468)*, vol. 1, pp. 715-719, 2003.

[13] J. F. Silva, "Input filter design for power converters" Texto complementar da disciplina SAA, Online, March 2011,
https://fenix.tecnico.ulisboa.pt/downloadFile/3779578920509/input%20LC%20filters.pdf.

[14] C. Mi, H. Bai, C. Wang, and S. Gargies, "Operation, design and control of dual h-bridge-based isolated bidirectional DC-DC converter", *IET Power Electronics*, vol. 1, no. 4, pp. 507-517, 2008.

[15] G. Paraiso, S. Pinto, and F. Silva, "Modelling and nonlinear control of Dual-Active Bridge converters for DC microgrids", *IECON 2019 - 45th Annual Conference of the IEEE Industrial Electronics Society*, pp. 1850-1855, 2019.

[16] A. C. Baptista, C. F. Fernandes, J. T. Pereira, and J. J. Paisana, *Fundamentos de Eletrónica*, chapter 6, pp. 458-474, Lidel - edições técnicas, lda, December 2012.

[17] C. F. Fernandes, Integrated electrical systems of solar photovoltaic technology, Lecture 5 - Week3, Slides, 2019.

[18] *ALL-BLACK CS6P-260M—265M*, Canadian Solar Inc., December 2014.

[19] A. Djilali, B. Hemici, and A. Yahdou, "Modified perturb and observe MPPT control for avoid deviation in photovoltaic systems", *Journal of Electrical Engineering*, vol. 17, pp. 28-37, January 2017.

[20] N. Femia, G. Petrone, G. Spagnuolo, and M. Vitelli, "Optimization of perturb and observe maximum power point tracking method", *IEEE Transactions on Power Electronics*, vol. 20, no. 4, pp. 963-973, 2005, doi: 10.1109/TPEL.2005.850975.

[21] H. K. Khalil, *Nonlinear systems, 3rd edition*, New Jersey, USA: Prentice Hall, 2002.

[22] G. M. Paraíso, "Design of control strategies for low voltage DC residential grids", Master's thesis, Instituto Superior Técnico, Universidade de Lisboa, Nov. 2018.

[23] W. Xiao, *Photovoltaic Power System*, chapter 6 - Dynamic Modelling, pp. 173-197, John Wiley & Sons, Ltd, 2017, ISBN 9781119280408, doi: 10.1002/9781119280408.ch6.